

# Notice

This manuscript is a non-peer reviewed preprint submitted to EarthArXiv. It has been submitted for publication to GJI on 27/10/2020 with reference ID #GJI-20-1072. Newer versions may be moderately different with slight variations in content.

## Manuscript details

Title: Future magnitude 7.5 earthquake offshore Martinique: Spotlight on major source-related factors of ground-motion variability

Authors: Elif ORAL (IPGP and Geoazur) and Claudio Satriano (IPGP)

Contact: [elif.oral@geoazur.unice.fr](mailto:elif.oral@geoazur.unice.fr)

# 1 **Future magnitude 7.5 earthquake offshore Martinique:** 2 **Spotlight on the main source features controlling ground** 3 **motion prediction**

4 Elif Oral<sup>1,2</sup> and Claudio Satriano<sup>1</sup>

<sup>1</sup> *Université de Paris, Institut de physique du globe de Paris, CNRS, F-75005 Paris, France*

<sup>2</sup> *Université Côte d'Azur, IRD, CNRS, Observatoire de la Côte d'Azur, Géoazur, France*

5 4 May 2021

## 6 **SUMMARY**

7 The eastern offshore of Martinique is one of the active areas of the Lesser Antilles Sub-  
8 duction Zone (LASZ). Although its seismicity is moderate compared to other subduction  
9 zones, LASZ is capable of generating a M 7+ interplate earthquake and recent studies and  
10 historical events, such as the M8 1839 and M 7-7.5 1946 earthquakes, confirm this possibil-  
11 ity. Given the high risk that Martinique can face in case of unpreparedness for such a M 7+  
12 earthquake, and the lack of a regional seismic hazard study, we investigated through numeri-  
13 cal modelling how ground motion can vary for a hypothetical  $M_w$  7.5 interplate earthquake.  
14 Our main objective is to highlight the major factors related to earthquake source that can  
15 cause the highest variation in ground motion at four broadband seismic stations across Mar-  
16 tinique. For this purpose, we generated 320 rupture scenarios through a fractal kinematic  
17 source model, by varying rupture directivity, source dimension, slip distribution. We com-  
18 puted the broadband ground motion (0.5-25 Hz) by convolution of source-time functions  
19 with Empirical Green's Functions (EGFs), that we selected from the analysis of moderate  
20 events (M 4-4.5) recorded in the area of interest since 2016 by the West Indies network.  
21 We found that the fault geometry and the spatial extension of the largest slip patch are the  
22 most influential factors on ground motion. The significance of the variation of the predicted  
23 ground motion with respect to ground motion prediction equations (GMPEs) depends on

the evaluated frequency of ground motion and on the station. Moreover, we concluded that the EGF selection can be another significant factor controlling the modelled ground motion depending on station. Our results provide a new insight for the seismic source impact on ground motion across Martinique and can guide future blind seismic hazard assessment studies in different regions.

**Key words:** Strong ground motion, Fault slip, Rupture propagation, Source time functions, Synthetic seismograms

## 1 INTRODUCTION

Martinique is located on the Lesser Antilles Subduction Zone (LASZ, Fig. 1), that is moderately active but capable of generating a  $M > 7$  interplate earthquake (e.g., [Feuillet et al. 2011](#)). LASZ is formed by the subduction of the Atlantic oceanic lithosphere under the Caribbean plate at a relatively slow convergence rate of 18 mm per year ([DeMets et al. 2010](#)). Martinique island is part of the north-south trending magmatic arc of LASZ. The seismicity of LASZ can be divided into: 1) flat-thrust interplate events above approximately 50 km in the fore-arc; 2) deep intraslab events in the back-arc; 3) intraplate events within the Caribbean Plate ([Russo et al. 1992](#); [Laigle et al. 2013](#); [Ruiz et al. 2013](#)). The scarcity of large ( $M > 7$ ) interplate thrust earthquakes in LASZ implies an unusual strain release compared to other subduction zones ([Russo et al. 1992](#)). Nonetheless, past studies ([Ruiz et al. 2013](#); [Laigle et al. 2013](#); [Weil-Accardo et al. 2016](#)) proposed that LASZ has high potential to generate a megathrust earthquake: the seismogenic zone might extend to the mantle wedge, below the forearc, and moderate seismic activity at the base of the seismogenic zone can load shallower segments and initiate a larger mega-thrust event. A similar mechanism has been proposed for the Japan trench subduction zone, leading to the 2011  $M_w$  9 Tohoku earthquake ([Satriano et al. 2014](#); [Barbot 2020](#)). [Laigle et al. \(2013\)](#) and [Satriano et al. \(2014\)](#) point to the similarities between Japan trench and LASZ—such as the lack of tremors and very-slow-low-frequency earthquakes, and the sustained activity in the mantle wedge—to better understand the long-term seismic activity of LASZ. Indeed, the recent study of [Paulatto et al. \(2017\)](#), linking heterogeneity of  $V_p/V_s$  ratio to earthquake activity in

51 LASZ, supports the proposed tectonic explanation and the analogy between Japan Trench and  
52 LASZ.

53 Historical events in the region confirm the possibility of a mega-thrust earthquake genera-  
54 tion in LASZ. [Feuillet et al. \(2011\)](#) compiled the data from several reports and papers for all  
55 significant historical earthquakes in the Lesser Antilles. They concluded that the magnitudes  
56 of the 1839 and the 1946 earthquakes offshore Martinique (Fig. 1) should be in the range of  
57 7-8, based on regional intensity reports. Moreover, [Weil-Accardo et al. \(2016\)](#) studied the sea  
58 level changes over the last two centuries by analysing morphological changes of microatolls in  
59 eastern offshore Martinique. They underlined the strong possibility of magnitude 7 or more for  
60 both historical earthquakes.

61 Great population density in Martinique leaves it vulnerable to high risk in case of unpre-  
62 paredness for a  $M > 7$  earthquake ([Audru et al. 2013](#)). In the absence of a regional seismic  
63 hazard study, ground motion prediction by numerical modelling can guide future mitigation  
64 studies. The conventional approach in seismic hazard assessment is the use of ground motion  
65 prediction equations (GMPE) that provide estimation of peak ground motion at a distance ([Dou-  
66 glas 2003](#)). A GMPE is developed based on statistical data, and the paucity of large events in  
67 LASZ renders a regional GMPE development difficult in Lesser Antilles. Indeed, the only avail-  
68 able GMPE, the ‘B3’ model of [Beauducel et al. \(2011\)](#), is limited to events of magnitude less  
69 than 6.3. As an alternative to GMPE, numerical modelling offers the possibility of better under-  
70 standing the physical aspect of the phenomenon (i.e., earthquake source and wave propagation).  
71 It allows for testing the outcomes of different configurations, which is particularly important for  
72 moderately seismic areas such as LASZ.

73 The challenge in numerical modelling is the uncertainty associated with model or input  
74 parameters, in particular when working with limited knowledge on earthquake process. The  
75 uncertainty related to earthquake source parameters can bring significant variations in the mod-  
76 elled ground motion (e.g., [Ripperger et al. 2008](#); [Imperator & Mai 2012](#); [Spudich et al. 2019](#)).  
77 This impact is also valid in backward modelling. For example, as shown in [Ragon et al. \(2019\)](#)  
78 by their analyses on the 2016 Amatrice, Italy earthquake, accounting for uncertainties of only  
79 fault geometry can drastically control the estimated fault slip.

80 Our main objective is to identify the major factors related to earthquake source that con-  
81 trol the ground motion amplitudes in Martinique during a potential  $M_w$  7.5 interplate thrust  
82 earthquake. Within this objective, we prepared 320 rupture scenarios by varying kinematic fea-  
83 tures of the target hypothetical earthquake. For each scenario, we coupled fault rupture with  
84 Empirical Green's Functions (EGF) for seismic wave propagation, and predicted broadband  
85 ground motion (0.5-25 Hz) at four stations of Martinique. Past studies (e.g., [Ameri et al. 2009](#);  
86 [Hartzell et al. 2002](#); [Pacor et al. 2017](#); [Sørensen et al. 2007](#); [Wang et al. 2009](#); [Withers et al.](#)  
87 [2019](#)) underlined the significant effect of source parameters on ground motion—for example,  
88 spatial variations of ground motion amplitudes due to rupture directivity or the location of slip  
89 asperities—, and the necessity of considering the variability of source parameters when mod-  
90 elling ground motion. Here, we take forward these studies by considering a comprehensive set  
91 of source parameters and performing analyses in a broader frequency range.

92 The secondary objective is to test the role of EGF selection on predicted ground motion. The  
93 EGF approach emerges as a powerful method to model broadband ground motion, especially  
94 when no detailed knowledge on propagation path is available, as revealed by many applications  
95 in the literature (e.g., [Kamae & Irikura 1998](#); [Pulido et al. 2004](#); [Causse et al. 2009](#); [Courboux](#)  
96 [et al. 2010](#); [Del Gaudio et al. 2018](#)). It also takes into account possible site effects (except for  
97 soil non-linearity) and provides full time histories of ground motion, differently than GMPEs.  
98 On the other hand, among the applications in actively seismic areas, EGFs can be selected from  
99 foreshocks or aftershocks of a specific earthquake (e.g., [Del Gaudio et al. 2015](#); [Dujardin et al.](#)  
100 [2016](#)). Here, we study a moderately-active zone with no successive recordings of such smaller  
101 events. In this case, selected events can differ more by several aspects such as seismic moment,  
102 stress drop, hypocentre location, etc. As [Pavic et al. \(2000\)](#) denoted, due to such differences  
103 between selected EGFs, further variation in ground motion can arise from the EGF method  
104 itself. Therefore, we also questioned the influence of EGF selection on ground motion.

105 Scoping these two objectives, the paper is structured as follows: 1) we detail the methods  
106 that we used for modelling source kinematics and wave propagation; 2) we explain how we  
107 constructed the set of earthquake scenarios and selected moderate earthquakes to employ as  
108 EGF; 3) we address the following three questions, respectively: 'Which aspect(s) of the source

109 control the ground motion, and why?'; 'How important is such a source impact on ground  
110 motion with respect to the GMPE?'; 'Is the EGF selection another significant factor to account  
111 for ground motion prediction?'; 4) we discuss the limitations of our study and present the main  
112 conclusions.

## 113 2 METHODS

114 We model the target interplate  $M_w$  7.5 earthquake by using the kinematic source model of  
115 Ruiz's Integral Kinematics (RIK, [Ruiz et al. 2011](#)). RIK model generates, for an earthquake  
116 with a prescribed seismic moment, a stochastic slip distribution along with the full slip history  
117 —the source-time functions (STF)— at each node of a discretised fault plane. We convolve the  
118 output STFs with empirical Green's functions (EGFs) to compute ground motion at four stations  
119 of Martinique. In the following are given the main features of the RIK and EGF methods,  
120 respectively.

### 121 2.1 Ruiz's Integral Kinematics (RIK) model

122 We performed kinematic rupture modelling by using the RIK model implementation of [Gallovíč](#)  
123 ([2016](#)). Slight modifications of the original RIK method issued by this implementation are also  
124 present here. The numerical tool that we used is an open source code (see [Data and resources](#)).

125 RIK is a composite model that describes an earthquake as a hierarchical set of smaller  
126 earthquakes, by definition of [Frankel \(1991\)](#). The essential idea behind the development of  
127 composite models is to represent the seismicity as a cascade of sub-sources standing for a wide  
128 range of wavelengths ([Andrews 1980](#)), and to mimic the high-frequency  $\omega^{-2}$  decay ( $\omega$ , being  
129 the angular frequency) of far-field displacement spectrum in observations ([Aki 1967](#); [Brune](#)  
130 [1970](#)), and in dynamic models of circular cracks (e.g., [Madariaga & Ruiz 2016](#)). A detailed  
131 review on the evolution of composite models can be found in [Ruiz et al. \(2011\)](#).

132 The number of sub-sources depends on their size, which follows a fractal distribution: the  
133 number of sub-sources with radius greater than a given size is:

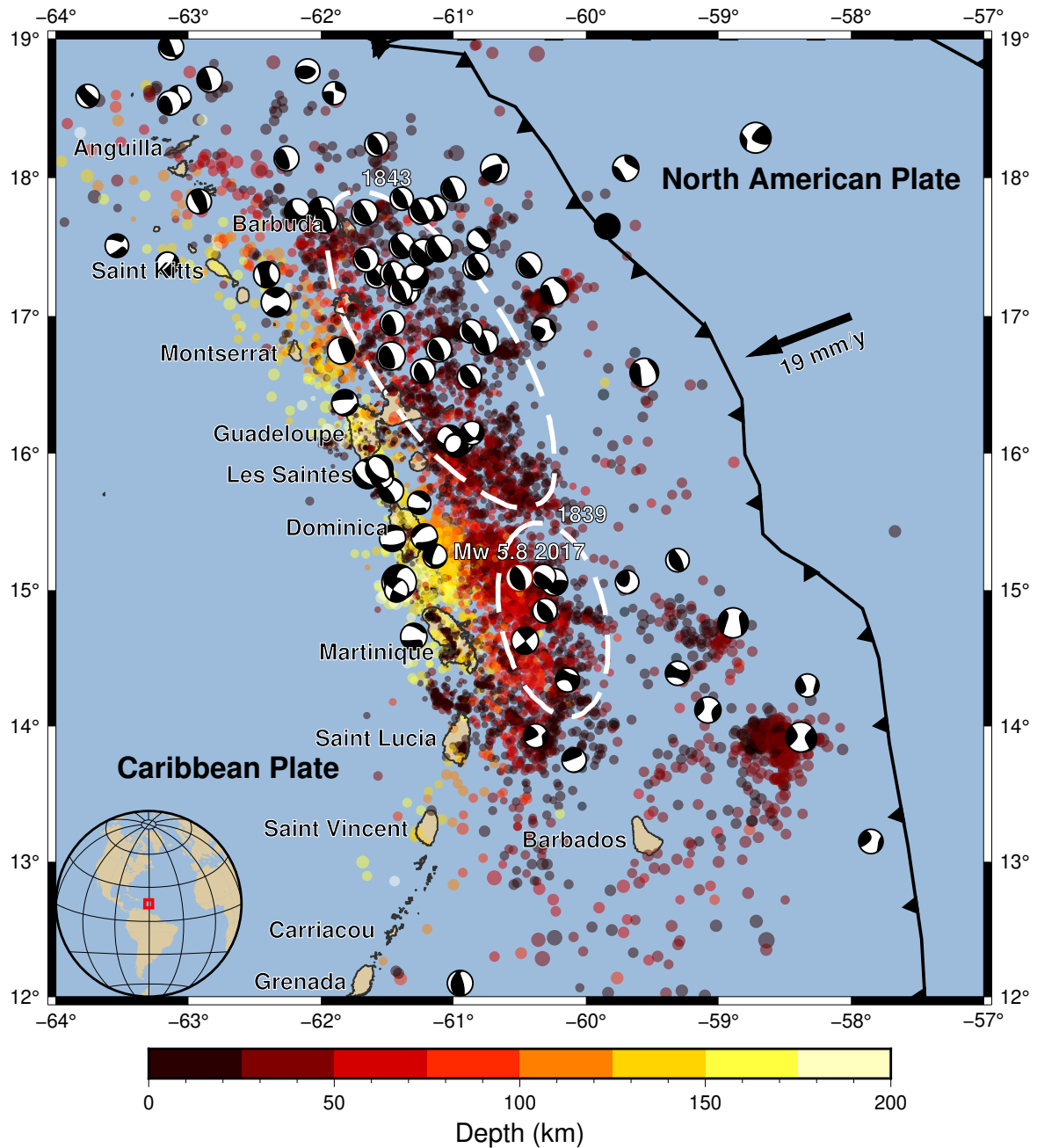


**Figure 1.** Seismicity of the Lesser Antilles Subduction Zone (LASZ). The dashed ellipses indicate the rupture area of the 1839 and 1843 earthquakes, inferred by [Feuillet et al. \(2011\)](#). The circles, coloured by depth, are the hypocentres from the unified catalogue of the IGP French observatories ([OVSG & OVSM 2020](#)), between 01/01/2014 and 31/12/2019. Focal mechanisms, from GlobalCMT ([Dziewonski et al. 1981; Ekström et al. 2012](#)), are for  $M5+$  earthquakes between 1978 and 2019. Focal mechanism for the 03/02/2017  $M_w$  5.8 event is from SCARDEC ([Vallée et al. 2011](#)).

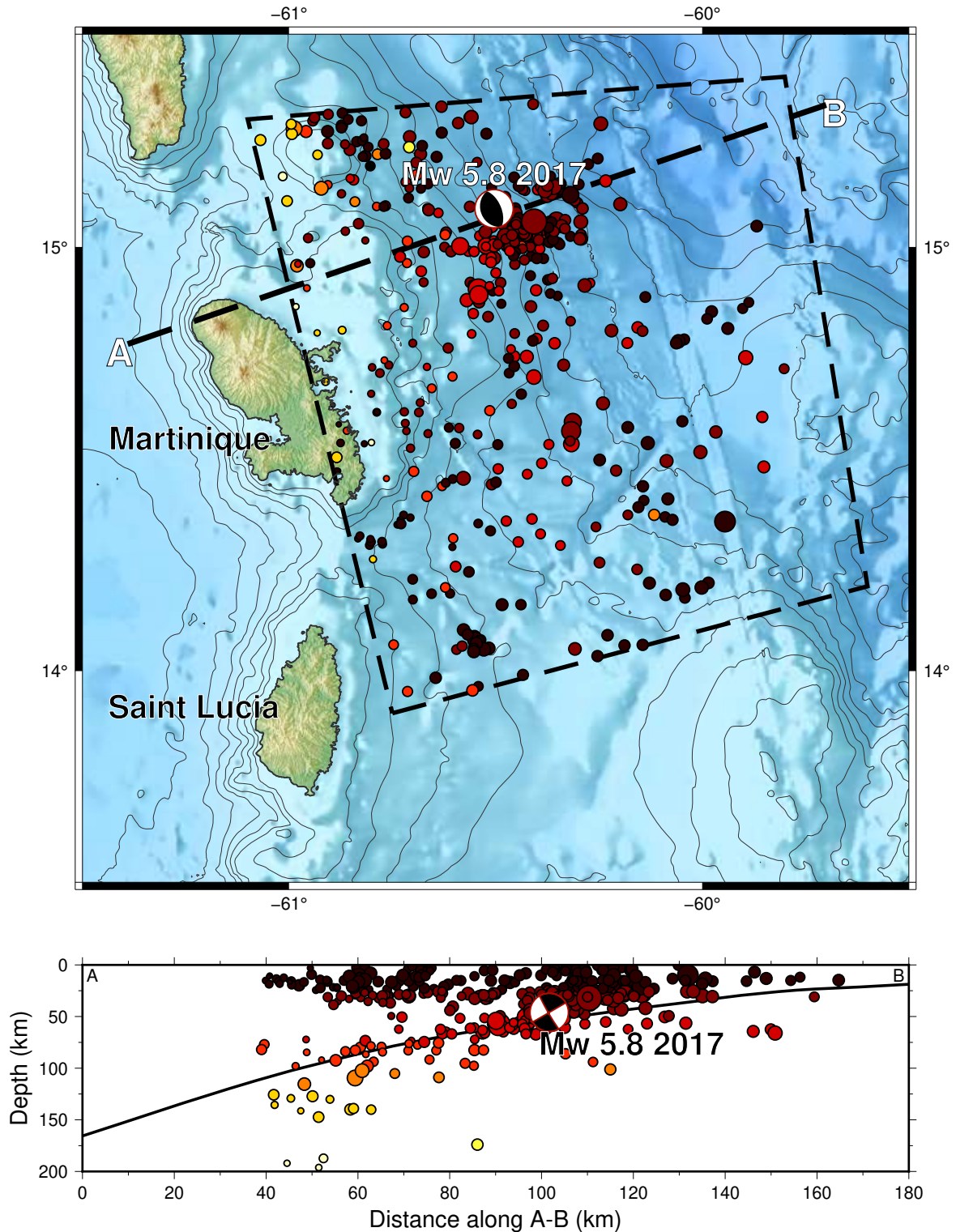


**Figure 2.** Seismic catalogue selected for this study. The dashed polygon represents the geographical selection; hypocentres within this polygon are only of those recorded by the four broadband stations in Martinique. These hypocentres are also shown on the vertical cross-section, along with the slab model of [Paulatto et al. \(2017\)](#). Focal mechanism for the 03/02/2017  $M_w$  5.8 event is from SCARDEC ([Vallée et al. 2011](#)).



$$N = \sum_{i=SUB_{min}}^{SUB_{max}} (2i - 1) \frac{L}{W} \quad (1)$$

134 where  $L$  is fault length;  $W$  is fault width;  $SUB_{min}$  and  $SUB_{max}$  are lower and upper limits of  
135 the ratio of fault width to sub-source diameter, respectively.

Each sub-source is a circular fault, or crack—by definition of [Eshelby \(1957\)](#)—that is associated with a slip function of  $\Delta u$ , as follows:

$$\Delta u(r) = \frac{24}{7\pi} \frac{\Delta\sigma}{\mu} \sqrt{R^2 - r^2} \quad (2)$$

136 where  $\Delta\sigma$  is the static stress drop;  $\mu$  is the shear modulus;  $r$  is the radial distance to the sub-  
137 source centre; and,  $R$  is the sub-source radius. The formula is valid for  $r < R$ ; slip is zero  
138 outside the crack.

139 In the RIK model, the  $\omega^{-2}$  decay results from imposing a slip-velocity function with a scale-  
140 dependent rise time  $\tau(R)$  ([Ruiz et al. 2011](#)):

$$\tau(R) = \begin{cases} \frac{\alpha L_0}{V_r}, & \text{if } 2R > L_0 \\ \frac{\alpha(2R)}{V_r}, & \text{if } 2R \leq L_0 \end{cases} \quad (3)$$

141 where  $R$  is the sub-source radius,  $\alpha$  is a constant, that we set to 1 in this study;  $L_0$  is a threshold  
142 of pulse width; and,  $V_r$  is the rupture speed.

143 The scale dependency of rise time only applies for the sub-sources with diameter smaller  
144 than  $L_0$ . This feature implies a low-pass filtering effect on the final slip spectrum.

145 The total slip rate of the modelled earthquake is obtained by summing the slip-rate contri-  
146 bution of each sub-source. More details on the method can be found in [Ruiz et al. \(2011\)](#).

## 147 **2.2 Empirical Green's function (EGF)**

### 148 *2.2.1 Formulation*

149 We use the Empirical Green's Function (EGF) method ([Hartzell 1978](#); [Irikura 1986](#)) to model  
150 seismic wave propagation. This technique starts from the representation theorem of [Aki &](#)  
151 [Richards \(2002\)](#), which establishes a relationship between a fault rupture and the associated  
152 ground motion, based on Betti's theorem. The displacement, in the direction  $\vec{x}_n$ ,  $u_n$ , at position

153  $x$ , and time  $t$ , can be related to a discontinuity in the  $\vec{x}_p$  direction of a fault plane  $\Sigma$  by the  
 154 following integral:

$$u_n(x, t) = \int_{\Sigma} m_{pq}(\xi, \tau) * G_{np,q}(\xi, \tau; x, t) d\Sigma \quad (4)$$

155 where  $\mathbf{m}_{pq}$  is the moment density tensor;  $\mathbf{G}$  is the derivative of the Green's function tensor  
 156 with respect to the direction  $\vec{x}_q$  (along which the moment arm, or force separation, extends —  
 157 seismic source is represented by a force couple here); and the symbol  $*$  denotes time convolu-  
 158 tion.

159 Assuming that fault is embedded in a linearly elastic, isotropic medium, and each fault point  
 160 has the same slip-time dependency, the moment density tensor can be simplified as follows:

$$m_{pq} = \mu(\xi) s(\xi, \tau) (\vec{s}_p \vec{n}_q + \vec{s}_q \vec{n}_p) \quad (5)$$

161 where  $\mu$  is the shear modulus;  $s$  is the slip function; and  $\vec{s}$  and  $\vec{n}$  are the unit slip and fault-  
 162 normal vectors, respectively, and the term between parentheses represents the focal mechanism  
 163 of the causative fault.

164 Assuming that the radiated wave lengths are much greater than the fault dimension, eq. 4  
 165 can be written as follows:

$$u_n(x, t) = \int_{\Sigma} m_{pq}(\xi, \tau) d\Sigma * G_{np,q}(\xi, \tau; x, t) \quad (6)$$

166 When replacing the integral of the above equation with the seismic moment of a real —  
 167 EGF— event,  $M_0^{EGF}$ , it is possible to express the displacement-time history of an EGF event  
 168 by the following convolution:

$$u_n^{EGF}(x, t; \xi_0, \tau_0) = M_0^{EGF} (\vec{s}_p \vec{n}_q + \vec{s}_q \vec{n}_p) H(\tau - \tau_0) * G_{np,q}(\xi_0, \tau_0; x, t) \quad (7)$$

169 where  $\mathbf{H}$  is the unit Heaviside function that stands for source-time function based on the as-  
 170 sumption that the recorded wave periods are greater than rupture duration: Such an assumption

171 means that the source is treated as a true point source — that has a negligible extent;  $\xi_0$  and  $\tau_0$   
 172 are the hypocenter and the origin time of the EGF event.

173 We solve the displacement of the target event by the variational formulation of eq. 6 for a  
 174 discretized fault plane as follows:

$$u_n(x, t) = \sum_{ij} \mu^{ij} \cdot l \cdot w \cdot S^{ij} (\vec{s}_p \vec{n}_q + \vec{s}_q \vec{n}_p)^{ij} * G_{np,q}^{ij}(\xi, \tau; x, t) \quad (8)$$

175 where  $l$  and  $w$  correspond to length and width of the unit area of the discretized fault plane,  
 176 respectively;  $S$  stands for the slip amplitude that is associated with the grid point ( $ij$ ).

177 Assuming the same focal mechanism between the EGF and target events, and the same  
 178 Green's function term for each fault segment, we can solve the above equation by using the  
 179 EGF recording. Replacing the focal mechanism and Green's function term based on eq. 7, we  
 180 rewrite the displacement of target event as follows:

$$u_n(x, t) = \sum_{ij} \frac{\mu^{ij} \cdot l \cdot w \cdot \tilde{S}^{ij}}{(M_0^{EGF})^{ij}} * (u_n^{EGF})^{ij}(x, t; \xi, \tau) \quad (9)$$

181 In this new formulation,  $\tilde{S}$  stands for the slip function of the target event that is deconvolved  
 182 by the step function of EGF.

183 The detailed explanation of the assumptions and derivation of above formula can be found  
 184 in [Aki & Richards \(2002\)](#); [Hutchings & Viegas \(2012\)](#).

185 We set the fault discretisation after the assumption of self-similarity between EGF and target  
 186 events ([Aki 1967](#)), which, in this definition, implies a similar stress drop for the small and  
 187 large earthquakes, and proportionality between slip and rupture length. The following equation  
 188 provides the scale factor between EGF and target event based on seismic moment:

$$n = \frac{L}{l} = \frac{W}{w} = \left( \frac{M_0^{target}}{M_0^{EGF}} \right)^{1/3} \quad (10)$$

189 where  $L$  and  $W$  are the fault length and fault width of the target event, respectively;  $l$  and  $w$  are  
 190 the length and width of unit area of the fault grid, respectively;  $M_0^{target}$  is the seismic moment  
 191 of target event.

192 To satisfy the assumption of similarity between EGF and the target event in eq. 9, the two

193 events should share the characteristics of focal mechanism, location and stress drop. Based on  
 194 the applications of [Del Gaudio et al. \(2015, 2018\)](#), an earthquake should satisfy the following  
 195 criteria to be used as EGF: 1) its location should be close enough to that of the target event;  
 196 2) its focal mechanism should be compatible to that of the target event (difference of faulting  
 197 angles must be less than  $15^\circ$  and  $30^\circ$  for dip and strike, respectively); 3) its magnitude should  
 198 allow for a sufficient signal-to-noise ratio; and, at the same time, it should be at least 2 points  
 199 smaller than the target magnitude to comply with the point source assumption in eq. 7.

### 200 2.2.2 *Single-EGF vs Multi-EGF approaches*

201 The difference between the single- and multi-EGF approaches lies in the way one associates  
 202 the grid points of the fault plane with EGF(s): in the single-EGF approach, all the grid points  
 203 use the same EGF for convolution; in the multi-EGF approach, the nearest EGF to grid point is  
 204 used.

205 The multi-EGF approach can provide a better approximation of observations, as evidenced  
 206 by past studies ([Del Gaudio et al. 2015](#); [McGuire & Ben-Zion 2017](#); [Del Gaudio et al. 2018](#)). As  
 207 mentioned in [Introduction](#), in case of scarcity of successive recordings, the difference of focal  
 208 mechanism between the potential EGF events can critically increase such that EGF selection can  
 209 become another factor causing further variation in predicted ground motion. Therefore, given  
 210 the moderate seismicity of the studied zone, we considered both approaches in our analyses for  
 211 further comparison.

212 The multi-EGF approach requires a few corrections to bring all the EGFs to an equivalent  
 213 energy level and to account for differences between  $d^{point}$  (distance between station and grid  
 214 point) and  $d^{hypo}$  (distance between station and EGF hypocentre). We apply the following steps:

- 215 (i) adjustment of EGF spectra to the same shape (see section [3.3.1](#));
- 216 (ii) correction of differences in geometrical spreading: each convolution term, for each grid  
 217 point, is multiplied by  $d^{point}/d^{hypo}$ ;
- (iii) time shift correction: for each grid point, the source time function is shifted by:

$$t_{shift} = \frac{d^{point} - d^{hypo}}{\beta} \quad (11)$$

218 where  $\beta$  is average shear velocity. We use  $\beta = 4.5$  km/s, which is the average S-wave value from  
219 [Paulatto et al. \(2017\)](#) tomographic model in the 35-55 km depth range, where the synthetic faults  
220 are placed (see next section). The approximation in eq. 11 is sufficient when the EGF signals  
221 are dominated by S phase as in our study (see supporting figures in SI).

### 222 **3 EGF SELECTION AND EARTHQUAKE SCENARIOS**

223 In this section, we detail the procedure that we followed to select and correct the empirical  
224 Green's functions, and the preparation of earthquake scenarios.

#### 225 **3.1 EGF selection**

226 We extracted from the catalogue of the IGP Lesser Antilles observatories (see [Data and re-](#)  
227 [sources](#)) 423 events, between 01/01/2014 and 02/06/2018, whose epicentral locations are within  
228 a polygon offshore Martinique, as shown in Fig. 2. The depth of the selected events range be-  
229 tween 0 and 196 km. The events follow the general trends of the subduction zone in terms of  
230 depth: they advent as a mix of crustal, interface, and intraplate events (see the discussion in  
231 [Introduction](#)). Thus, it is important to closely examine their depth and focal mechanism.

232 The catalogue only comprises events which have been recorded at each of the four broad-  
233 band stations of the 'West Indies' network in Martinique (WI, [IPGP 2008c](#); [Anglade et al. 2015](#)):  
234 BIM, ILAM, MPOM, and SAM (station locations shown in Fig. 3). We have limited knowledge  
235 of site conditions, essentially based on geological maps ([Bureau de recherches géologiques et](#)  
236 [minières 2018](#)): ILAM and MPOM are on rock, BIM and SAM are on soft soils (SAM is on  
237 volcanic ash and pyroclastic flow deposits), and site effects can be present at BIM and ILAM.

238 Out of the 423 events in our initial catalogue, only three could be selected as EGFs, based  
239 on the criteria of distance, magnitude, and focal mechanism discussed in Section 2.2.1. In par-  
240 ticular, the desired EGFs: i) are located, in depth, in proximity to the subduction zone, as does  
241 the  $M_w$  5.8 earthquake of 03/02/2017 that we use as reference; ii) have a magnitude in the inter-  
242 val of 3.5-5.5; iii) have a focal mechanism of reverse faulting—, and sticking to the flat-thrust  
243 characteristic of our target event, we only searched for events in the depth range of 25-65 km.  
244 Fig. 3 show the locations of the three events that satisfy these criteria while Table 1 provides de-

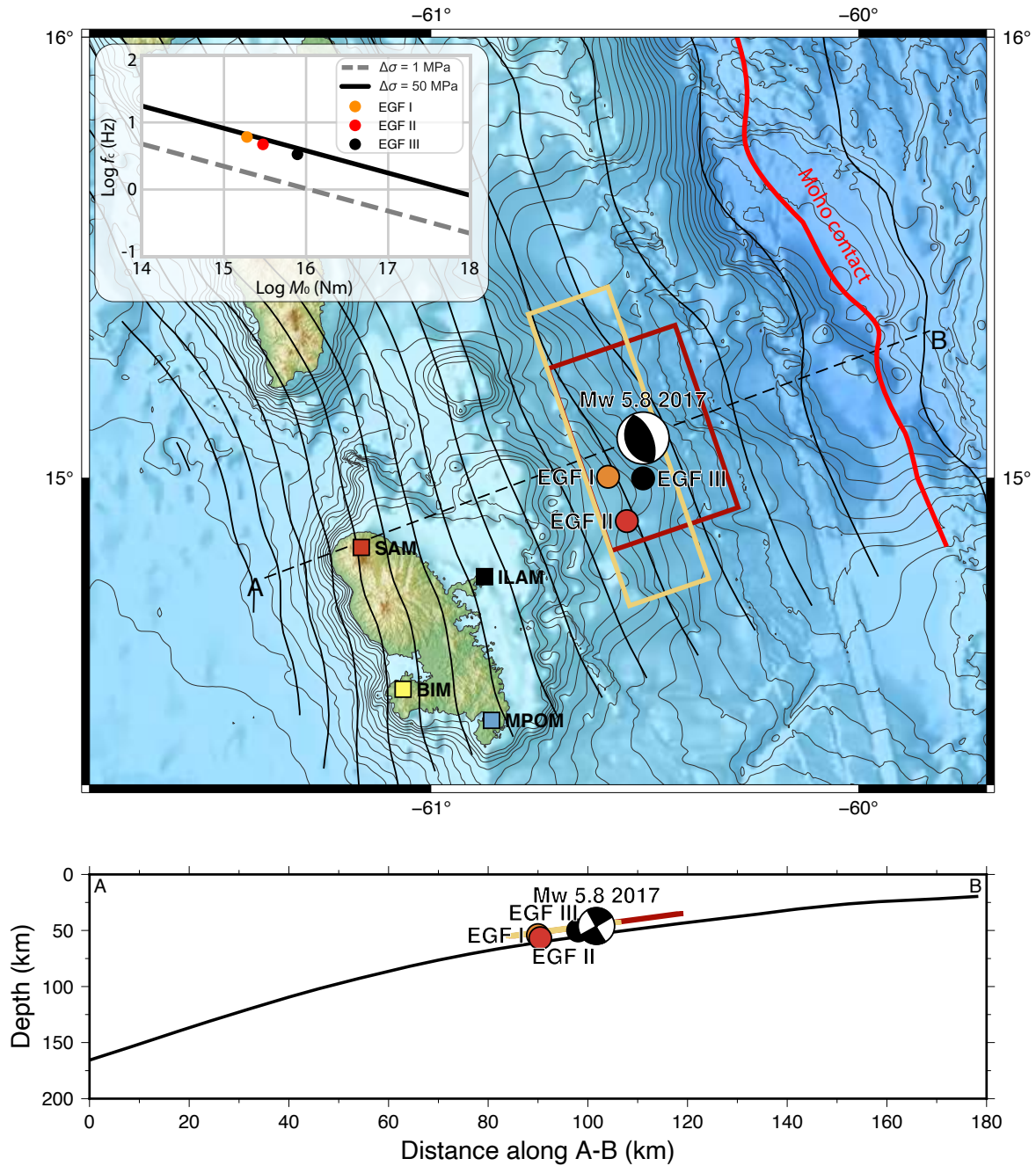


**Figure 3.** Source and station locations, and source properties of the selected EGFs. Map view of the four selected Martinique stations (WI network), the two fault geometries, the selected EGF events and the focal mechanism of the 2017  $M_w 5.8$  earthquake (top), and vertical section showing the EGFs and the 2017 focal mechanism (bottom). The slab geometry from [Paulatto et al. \(2017\)](#) is represented by contour lines (10 km depth interval) in map view and by the solid line in the depth section. The red line in the map view marks the contact between the overriding plate Moho and the slab, according to [Paulatto et al. \(2017\)](#). Embedded figure displays the corner frequency vs. seismic moment for each selected EGF.

**Table 1.** Catalogue information (ID, origin time, location,  $M_L$ ) for the EGFs used in this study and source properties ( $M_w$ ,  $f_c$ ,  $\Delta\sigma$ ) obtained from SourceSpec analysis.

EGF	Catalogue ID	Origin Time (UTC)	Lon. (° E)	Lat. (° N)	Depth (km)	$M_L$	$M_w$	$f_c$ (Hz)	$\Delta\sigma$ (MPa)
I	ipgp2016fkyaql	2016-03-17T18:31:26	-60.56	15.00	54.1	4.12	$4.1 \pm 0.2$	$6 \pm 2$	$40 \pm 28$
II	ipgp2017hushqx	2017-04-21T10:13:01	-60.54	14.90	56.8	4.82	$4.3 \pm 0.2$	$5 \pm 2$	$29 \pm 22$
III	ipgp2017sep1qt	2017-09-15T10:58:31	-60.50	15.00	50.0	5.04	$4.5 \pm 0.3$	$3 \pm 2$	$27 \pm 23$

245 tails on these EGFs. Details on the determination of focal mechanism of the catalogued events  
 246 are provided in SI. Moreover, note that, at the moment of submitting this article, a new solu-  
 247 tion for EGF II was made available in the catalogue—event ipgp2017hushqz, see [Data and](#)  
 248 [resources](#)—, with a slightly different location; we tested the effect of using this new solution  
 249 on ground motion variation and verified the validity of the conclusions of the present work, as  
 250 detailed in SI.

251 We determined the source properties of the selected three events (moment magnitude, cor-  
 252 ner frequency and stress drop) by using the SourceSpec software ([Satriano 2020](#)). SourceSpec  
 253 calculates the earthquake source parameters for an event by inverting the S-wave displacement  
 254 spectra from the recordings of multiple stations. The mean values of source parameters are com-  
 255 puted by the average of the results of all the stations. The standard deviation of each parameter  
 256 is also calculated; it can increase due to certain factors such as local soil conditions and/or poor  
 257 signal quality at station. Therefore, we used all available data (stations from networks CU, G,  
 258 GL, MQ, NA, and WI; network information is detailed in [Data and resources](#)) and disregarded  
 259 the stations with relatively high deviation to increase the robustness of the solution. Table 1  
 260 also lists the results of moment magnitude  $M_w$ , corner frequency  $f_c$ , stress drop  $\Delta\sigma$  for each  
 261 selected EGF.

262 In the following, we will only consider moment magnitudes. Fig. 3 shows the relation be-  
 263 tween corner frequency and seismic moment of each event with respect to stress drop. The mean  
 264 stress drop of each EGF is between 25 and 50 MPa, and align considerably well in the diagram.

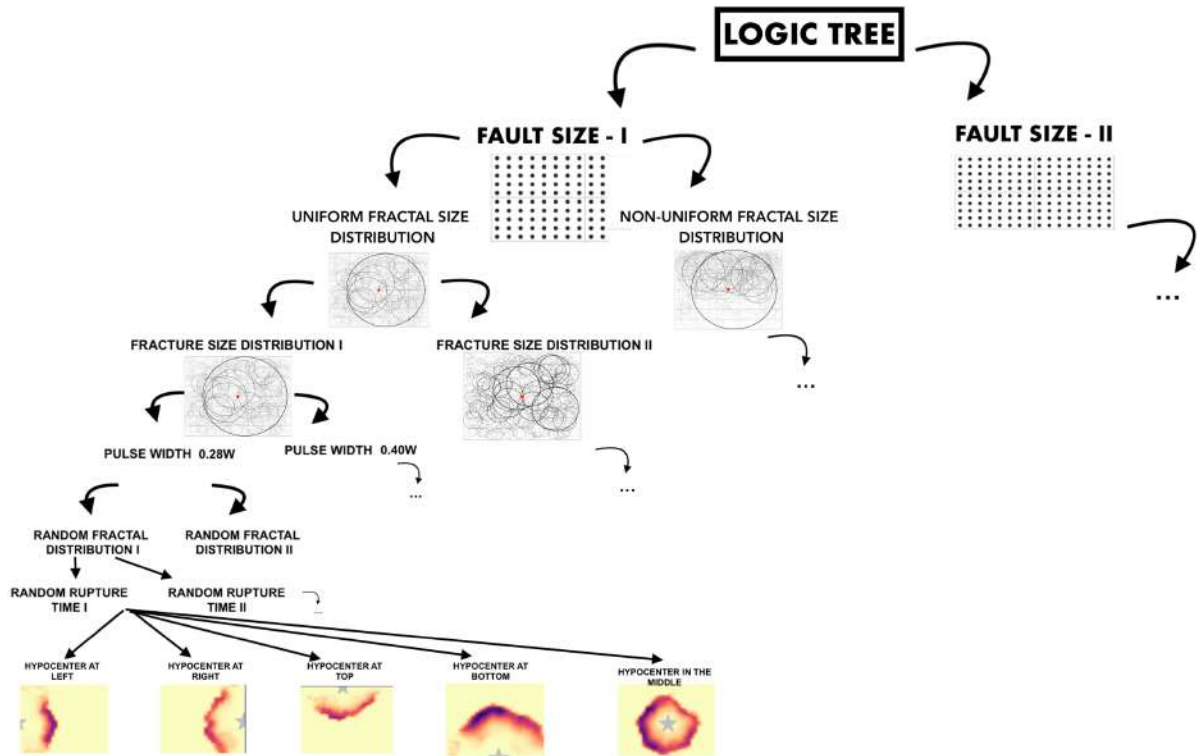


**Figure 4.** Illustration of the logic tree organisation for generating earthquake scenarios. Three dots indicate the repetition of sub-branches similar to those of neighbour branch.

## 3.2 Earthquake scenarios

We prepared a set of earthquake scenarios for an interplate  $M_w$  7.5 earthquake, comprising of 320 different kinematic rupture models. To take into account different aspects of source kinematics, we constructed a logic tree where each branch explores a different source parameter (Fig. 4). In the following, we briefly explain these aspects by hierarchical order.

### 3.2.1 Fault geometry

The logic tree starts with the main branches of fault geometry. We created two models: 1) a fault with a low aspect ratio (square-like) with dimensions of  $50 \text{ km} \times 40 \text{ km}$ ; 2) a fault with a high-aspect ratio (rectangular) with dimensions of  $80 \text{ km} \times 25 \text{ km}$ . We set the model dimensions based on the scaling law of seismic moment for a magnitude 7.5 event such that the two cases have the same rupture area.

We fixed the fault location and orientation based on a reference event, the 03/02/2017  $M_w$  5.8 earthquake (Fig. 3). The focal mechanism of this event was reported as reverse faulting



with strike, dip and rake angles of  $161^\circ$ ,  $30^\circ$  and  $94^\circ$ , respectively, and hypocentre is located at 46 km depth (SCARDEC data by Vallée et al. 2011). We set our maximum fault depth to 55 km in all cases, by respecting the past documentation on the seismogenic zone (e.g., Paulatto et al. 2017). As for the updip fault limit, we consider here a rupture occurring at the slab-mantle wedge interface, where most of the large M5+ interplate earthquakes and background seismicity occur (see Fig. 1), as also evidenced by Paulatto et al. (2017). Similarly to what happens for the Japan trench (Satriano et al. 2014), M7 earthquakes occurring deeper but closer to the coast, are susceptible to generate stronger ground motion. We defined the midpoint of the first type of fault geometry at the hypocentre coordinates of the 03/02/2017 event ( $15.090^\circ$  N,  $60.504^\circ$  W). In this way, the fault plane extends between 35-55 km and 42.5-55 km depths for the first and second types of geometries, respectively. Fig. 3 depicts the location of two fault geometries in map view and cross section. The alignment of fault planes are slightly shallower with respect to the slab, but in good agreement with the depth of recorded events.

### 3.2.2 *Spatial distribution of sub-sources*

We created two sub-branches to test the effect of using uniform or dip-varying spatial distribution of large sub-sources. In uniform-distribution model, we evenly distributed the sub-sources all over the fault plane; in dip-varying distribution model, we define the along-dip probability to have a sub-source as:

$$P(d) = \cos^9 \left( \frac{\pi d}{2W} \right),$$

where  $d$  is the along-dip distance and  $W$  is fault width:  $P(0) = 1$  at fault top;  $P(W) = 0$  at fault bottom. The power of nine was arbitrarily chosen to increase the relative probability close to the fault top with respect to the fault bottom. From this probability function, we define a sub-source size-dependent probability

$$\bar{P}(R, d) = P(d)^{\gamma(R)}$$

$$\gamma(R) = \frac{R - R_{min}}{R_{max} - R_{min}}.$$

Hence, for the largest sub-source, the probability density function equals  $P(d)$ ; and for the smallest one it equals 1, i.e., being uniform over the fault plane.

### 294 3.2.3 Sub-source size

295 We tested the effect of the presence of the largest sub-source, with diameter equal to fault  
 296 width. The first sub-branch allows for a relatively large range of sub-source sizes: the largest  
 297 and smallest radii equal 100 % and 5 % of fault width, respectively. We lowered the largest  
 298 radius to 50 % in the second group.

### 299 3.2.4 Pulse width, $L_0$

300 As mentioned in Section 2.1, this parameter produces a low-pass filtering effect on slip spec-  
 301 trum, and hence can influence the ground motion amplitude. We tested the power of such influ-  
 302 ence by adding two sub-branches: 1)  $L_0 = 0.28 \times W$ ; 2)  $L_0 = 0.4 \times W$ . The use of very small  
 303 values of  $L_0$  can lead to unrealistically high ground motion amplitudes, such as PGA exceeding  
 304 2 g; We opted for the  $L_0$  values for these two cases after a sensitivity analysis of the parameter  
 305 on PGA (detailed in SI).

### 306 3.2.5 Random parameters, $idum1$ and $idum2$

307 The numerical tool that we use incorporates two parameters,  $idum1$  and  $idum2$ , that control the  
 308 randomness of the spatial distribution of sub-sources and propagation of rupture front on fault  
 309 grid, respectively. We created two additional orders of sub-branches to account for each of this  
 310 randomness.

### 311 3.2.6 Rupture directivity

312 We created a last order of sub-branches to test the effect of rupture directivity, by varying the  
 313 hypocentre location. We prepared five cases based on the relative location of hypocentre on fault  
 314 plane: left, right, top, bottom, centre.

## 315 3.3 EGF correction and coupling with kinematic rupture model

### 316 3.3.1 EGF correction

317 We adjusted all selected EGFs to the same spectral shape that corresponds to a reference spec-  
 318 trum for a  $M_w$  4.3 event, with a seismic moment of  $3.6 \times 10^{15}$  Nm. The philosophy of EGF

319 correction is to reduce significant variation of ground motion amplitudes that can possibly arise  
320 from the difference of stress drop of selected EGFs ([Hutchings et al. 2007](#); [Del Gaudio et al.](#)  
321 [2015](#)). We set the corner frequency of the reference spectrum to the mean of EGFs' values, that  
322 roughly equals 5 Hz. For each station record of each EGF, the adjustment procedure applies as  
323 follows:

- 324 (i) computation of the Fourier transform of displacement;
- 325 (ii) conversion of displacement spectrum to seismic moment unit;
- 326 (iii) deconvolution (amplitude division) of the converted spectrum by Brune's spectrum that  
327 corresponds to the corner frequency and seismic moment of the uncorrected EGF—this step is  
328 similar to the application in [Causse et al. \(2017\)](#);
- 329 (iv) multiplication of the deconvolved spectrum with the mean seismic moment.

330 Generally, the EGF summation technique in eq. 9 is applied up to the EGF's corner fre-  
331 quency ([Hartzell 1978](#)), above which the solution has larger uncertainties. This is mainly be-  
332 cause the point-source assumption in eq. 7 is satisfied with a flat amplitude spectrum, while  
333 the observed spectrum is not flat above the corner frequency. The EGF deconvolution by a  
334 Brune's spectrum only partially recovers a flat amplitude spectrum: the Brune's model is not  
335 fully adequate in describing high-frequency radiation, since it assumes an instantaneous rupture  
336 on a circular fault, which is a good approximation only below the corner frequency ([Madariaga](#)  
337 [& Ruiz 2016](#)). For higher frequencies, the spectrum of any earthquake deviates—in amplitude  
338 and phase—from the Brune's model: the seismic radiation at high frequencies is inherently  
339 stochastic, since the different portions of the rupture interfere with each other. This stochas-  
340 tic behaviour is therefore still present after the Brune's spectrum deconvolution and the EGF  
341 summation can result in constructive/destructive interference above the corner frequency, de-  
342 pending on the high-frequency spectrum shape of the (corrected) EGFs. We further discuss the  
343 limitation arising from this application in next section.

344 It's worth noting that we preserve the attenuation information on the final spectrum by not  
345 including anelastic (and geometric) attenuation in the Brune's spectrum which is deconvolved in

346 step (iii). Final step of signal processing includes: removal of instrumental response, detrending,  
347 and band-pass filtering in the frequency band of 0.01-49 Hz.

348 Fig. 5a shows an example of spectral adjustment of EGF III for the north-south component  
349 of station BIM. All the spectra are smoothed with a Hanning window of the 5<sup>th</sup> degree. We  
350 see in the example that the spectrum is deamplified after correction at frequencies below the  
351 corner frequency of reference spectrum ( $\sim 5$  Hz) since the seismic moment of the uncorrected  
352 EGF is higher than the reference one. The flattening effect of EGF adjustment beyond corner  
353 frequency produces an amplification at frequencies above  $\sim 5$  Hz; however, due to the pre-  
354 served anelastic attenuation, the resultant spectrum still shows a decay for frequencies above  
355  $\sim 6$  Hz. The resulting signal in time domain depicts notable amplification—up to 2 times for  
356 peak values—throughout the signal duration due to correction, as shown in Fig. 5b.

### 357 3.3.2 Coupling with kinematic rupture model

358 We discretized the fault plane based on the ratio of seismic moment between the target and  
359 EGF events, that equals 40. Referring to eq. 10, our fault grid contains 1600 points ( $40 \times 40$  for  
360  $n = 40$ ) for all rupture models.

361 For each grid point, the corresponding source time function is convolved with the nearest  
362 EGF in 3D space. One example of such partition for the case of a fault with low-aspect ratio (the  
363 1<sup>st</sup> type of fault geometry in the logic tree) is given in SI (Fig. S1). We then made additional  
364 corrections as detailed in Section 2.2.2. The modelled ground motion at a station issued by the  
365 target earthquake equals the sum of the corrected convolutions. The velocity and density profile  
366 that we used is provided in SI.

367 The frequency band which we considered for ground motion modelling is 0.5-25 Hz, based  
368 on signal quality. We further analysed the signal-to-noise-ratio (SNR) of each EGF recordings  
369 for each station. Except for the cases with slightly lower SNR values, all the cases provide SNR  
370 values above 5 in the frequency band of 0.5-25 Hz. Therefore, we will refer to this frequency  
371 band in the evaluation of our ground motion models.

372 The main limitation of our modelling approach is that the EGF has a corner frequency of  
373 5 Hz, that is smaller than the above-mentioned resolution, 25 Hz. As detailed in the previous

## EGF III corrected for the NS component of station BIM

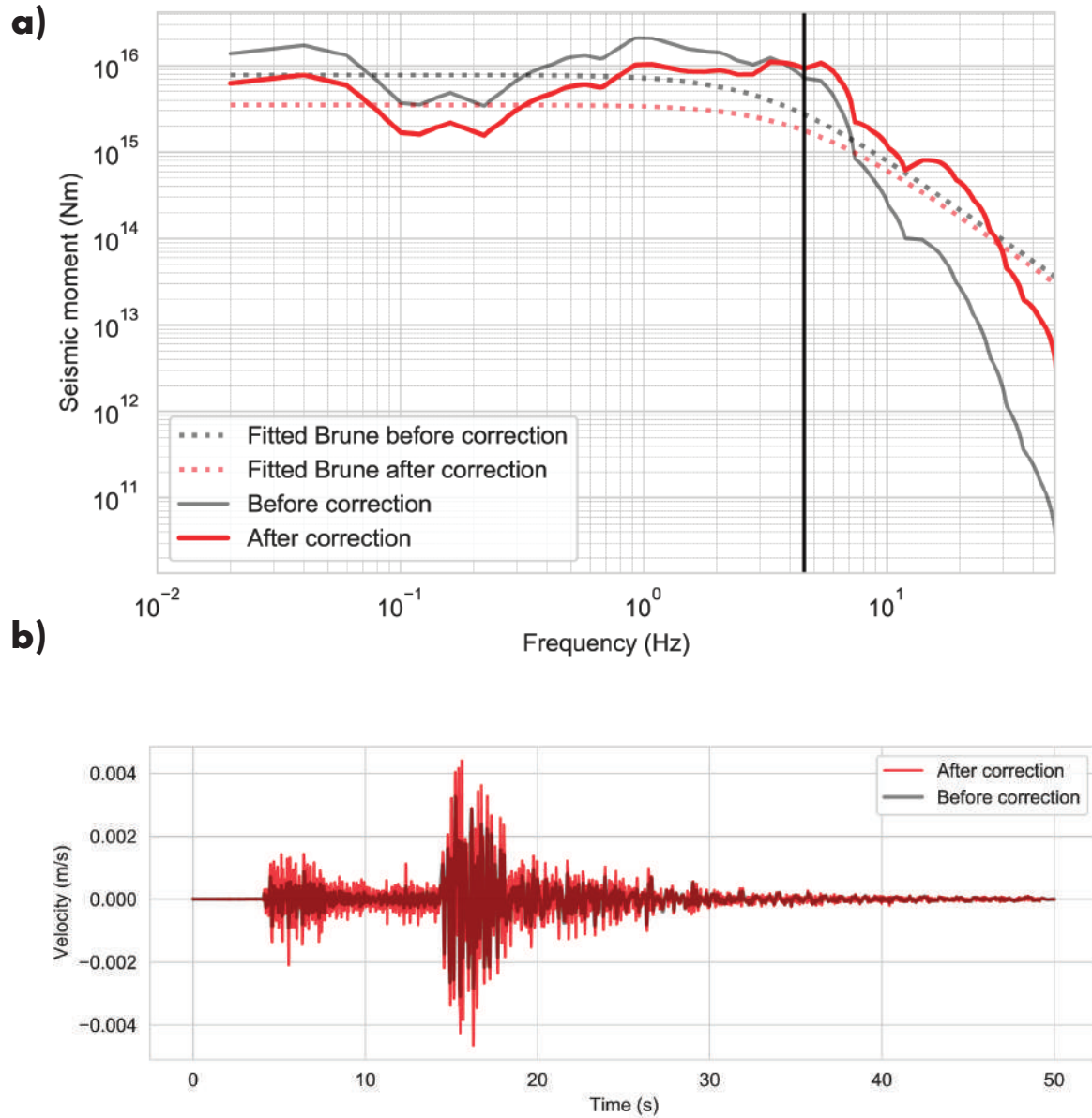


**Figure 5.** Example of EGF correction. a) Moment spectra of the north-south component of EGF III signal at station BIM before and after correction. b) Velocity-time histories before and after correction.

374 section, the EGF deconvolution by a Brune's spectrum does not mitigate interference effects  
 375 arising from rupture stochasticity and, hence, the uncertainties associated with the modelled  
 376 ground motion are higher above the EGF's corner frequency. [Causse et al. \(2009\)](#) discuss that  
 377 such stochastic effects can lead to overestimation of high frequency level of apparent source-  
 378 time function in case of constructive interference. Here we verified the lack of such artefacts in

our models as exemplified in SI, Fig. S2. We note and consider this limitation when interpreting  
our results in the following.

## 4 RESULTS

We evaluate the results for the 320 simulated scenarios, through the following parameters: peak-  
ground acceleration (PGA), spectral acceleration (SA) values at 1, 2 and 5 Hz, and Arias inten-  
sity. We made these analyses on the maximum of the three components. Lancieri et al. (2015)  
showed that these are the most influential parameters on seismic structural analysis.

### 4.1 Fault geometry and sub-source size control the ground motion prediction

The first question we wanted to address is: ‘Which aspect(s) of the source control the ground  
motion?’. To answer this question, we evaluated the model outputs by considering each branch  
of the logic tree (Fig. 4). To account for both amplitude and energetic content of the calculated  
ground motion, we disaggregated the simulation results based on PGA and peak Arias intensity.  
Fig. 6 shows disaggregation for station ILAM (the analyses on the other stations lead to the  
same conclusion, as shown in SI). Our analyses on all four stations highlight a distinctive clus-  
tering due to the fault geometry and sub-source size: a low aspect ratio of fault geometry brings  
relatively low energetic ground motion (cluster A); whereas, a high aspect ratio of fault geome-  
try together with smaller slip asperities—i.e., a rectangular fault where sub-sources larger than  
50% of fault width are forbidden—results in a notable amplification of peak ground motion  
(cluster B).

Such clustering implies a significant change of wave energy throughout the signal duration  
and in a broad frequency range (0.5-25 Hz). We picked a representative case from each of  
the above-mentioned two clusters A and B. We compared the two cases by acceleration-time  
histories, their Fourier amplitudes, and temporal change of Arias intensities. Fig. 7 displays  
this comparison for all stations. The cluster B case evicts a higher level of wave energy at all  
stations: PGA is approximately 2 times higher, and the peak Arias intensity can reach to 10  
times higher values for all stations.

We found that the combination of a fault geometry with a high aspect ratio and a spatially-

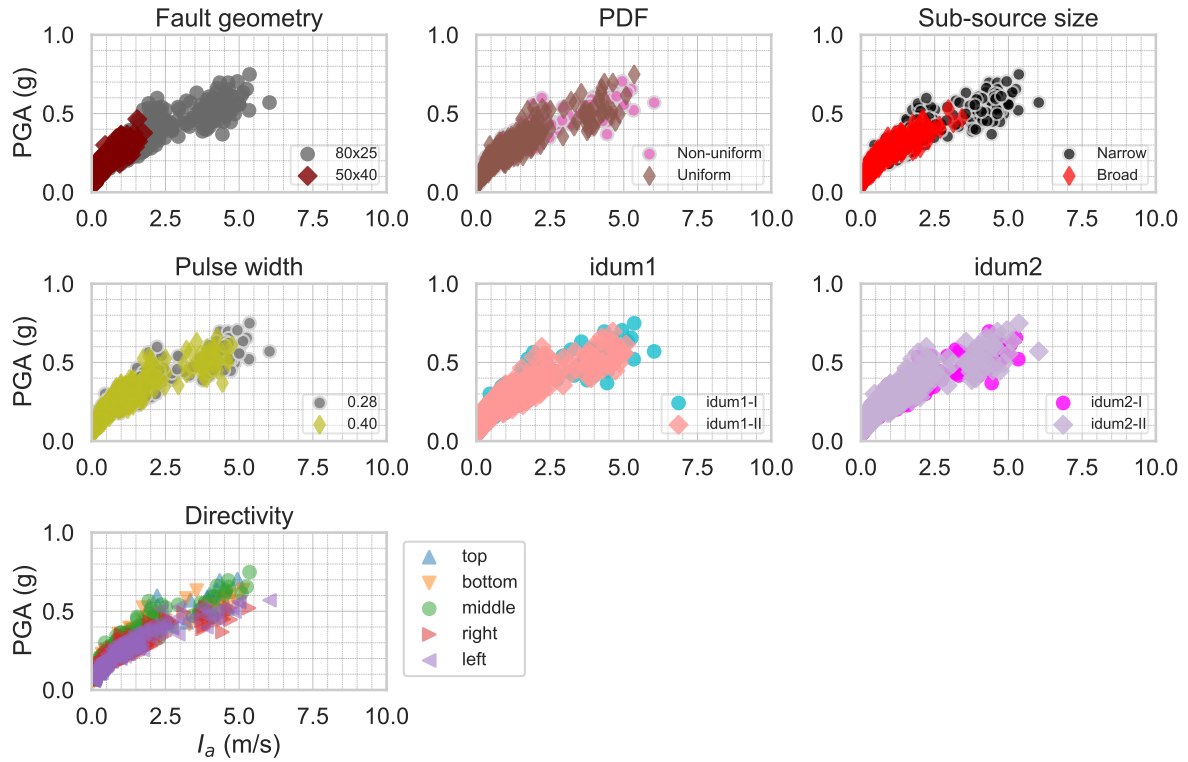


**Figure 6.** Disaggregation of computed ground motion by PGA and peak Arias intensity for station ILAM. We classified the results by different parameters in each diagram: by fault geometry, spatial distribution of sub-sources (PDF), sub-source size, pulse width, idum1, idum2, and directivity. The choice of fault geometry and sub-source size parameters are the causative factors of two distinct clusters, which we call ‘A’ and ‘B’.

406 condensed largest slip distribution, i.e., smaller patches with greater slip values, makes a double  
 407 effect of amplification of source energy; and, this double energy boost leads to the clustering of  
 408 ground motion. We compared the two clusters by sub-source distribution (a), final slip distri-  
 409 bution (b), and STF (moment-rate time function) and moment spectra (c) (Fig. 8). Our analysis  
 410 evidences that:

411 (i) The presence of the sub-source with a diameter equal to fault width (cluster A) results in a  
 412 spatially extensive slip asperity such that a significant part of the fault plane undergoes relatively  
 413 large slip. Yet, the lack of such big-size sub-source (cluster B) results in a slip distribution where  
 414 the largest values are spatially concentrated in relatively small patches. This leads to a partial  
 415 amplification of source energy in the whole frequency band, in particular above 1 Hz.

416 (ii) The fault geometry with high aspect ratio (cluster B) can result in a rupture propaga-

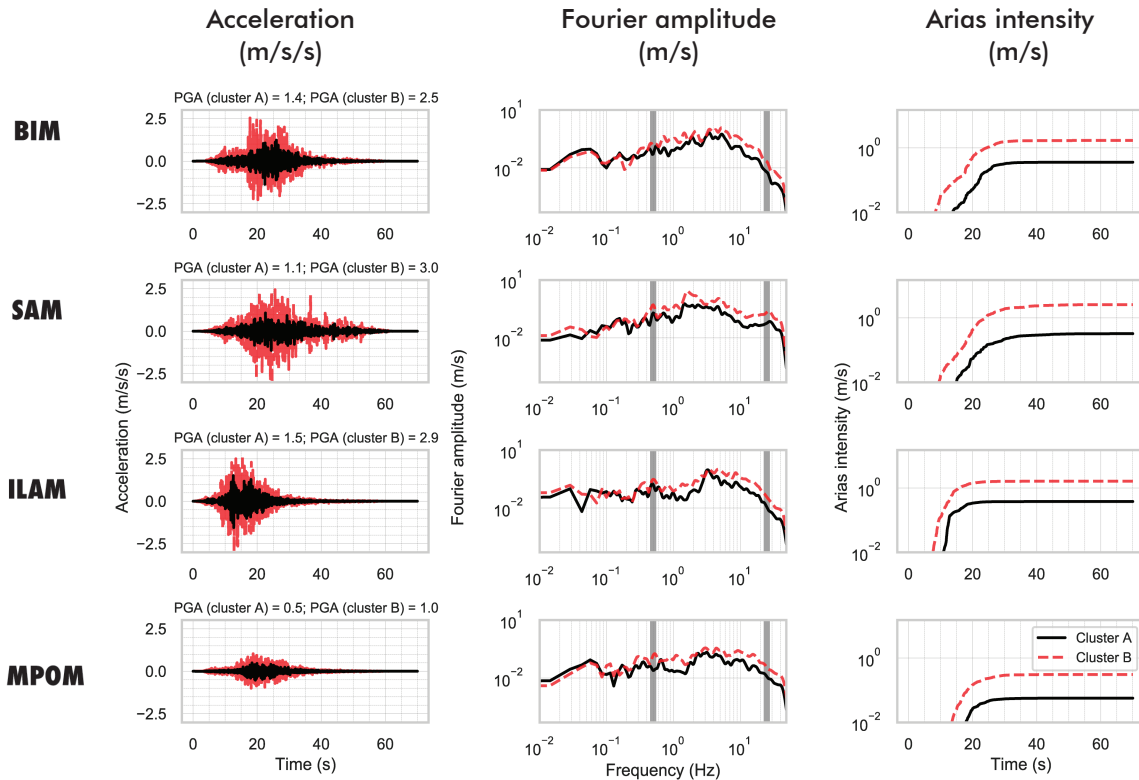


**Figure 7.** Comparison of acceleration-time histories (left panel), Fourier amplitude (middle panel), and Arias intensities (right panel) between cluster A (in black) and cluster B (in red) (see Fig. 6). We used the north-south component of signals in each comparison. Each row corresponds to the results of a station: BIM, SAM, ILAM, and MPOM, from top to bottom, respectively. The frequency band of 0.5-25 Hz is indicated by grey bars.

417 tion that is longer and in a composite source-time function with multiple peaks and shorter rise  
 418 time—individual slip-rate functions become spiky (short rise time) in the cluster B case, differ-  
 419 ently than the case of cluster A that has smooth STFs (see details in SI). This complexity also  
 420 partially contributes to the energy amplification in the whole frequency band.

#### 421 **4.2 Comparison with GMPE: source impact on ground motion determines the GMPE** 422 **compatibility**

423 The second question we wanted to address is: ‘How important is the source-related changes  
 424 in ground motion with respect to the GMPE?’. In previous section, we evidenced two clusters  
 425 of synthetic ground motion due to the differences of source definition. Here, we evaluate this  
 426 ground-motion clustering by referring to the compatibility of the modelled data with GMPE.



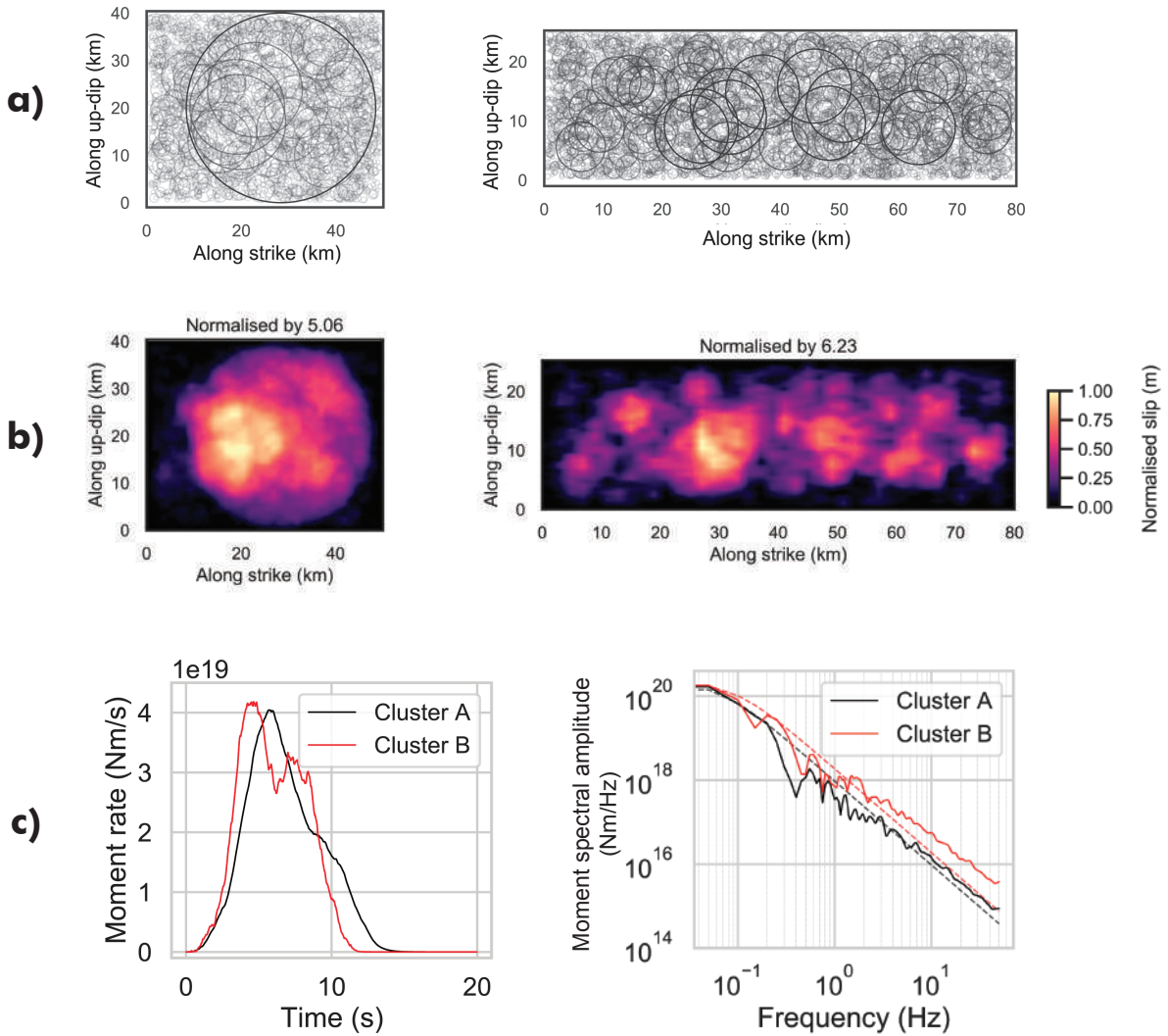


**Figure 8.** Comparison of source features of the two clusters shown in Fig. 6. a) Comparison of cluster A (left panel) and cluster B cases (right panel) by sub-source distribution. b) Same as a) for final slip distribution. c) Comparison of source-time function (left panel) and moment spectra (right panel) between cluster A (in black) and cluster B (in red) cases.

427 [Bozzoni et al. \(2011\)](#) compiled all the available databases in Eastern Caribbean Islands and  
 428 analysed different GMPEs that have been developed for other regions with similar seismotec-  
 429 tonic settings. They recommend the GMPE of [Zhao et al. \(2006\)](#) for the type of events we study  
 430 here, namely plate interface earthquakes with a reverse faulting mechanism. A similar conclu-  
 431 sion was made in a later study by [Douglas & Mohais \(2009\)](#). The GMPE of [Zhao et al. \(2006\)](#)  
 432 consists of four soil categories: rock, hard soil, medium soil, and soft soil. In the absence of a  
 433 detailed knowledge on site conditions, we have chosen the site condition of soft soil. We ver-

434 ified by using other site conditions that this choice only causes slight variations of amplitude  
435 and does not change our conclusions (see figures in SI).

436 The two clusters of synthetic ground motion have two different levels of ground motion  
437 amplitude by distance. The compatibility of these trends with GMPE for  $M_w 7.5$  strongly  
438 depends on frequency and station. Fig. 9 shows the comparison of synthetic ground motion and  
439 GMPE curves for spectral acceleration (SA) analyses at 1, 2, and 5 Hz. We make the comparison  
440 separately for each station, and the hypocentral distance at each simulation varies based on the  
441 definition of hypocentre. In general, cluster B is associated with higher amplitude of ground  
442 motion at all distances. At 1 Hz, the majority of the synthetic ground motion agrees well with  
443 GMPE for stations BIM and SAM; but, the ground motion at the same frequency is mostly  
444 underestimated for stations ILAM and MPOM. At 2 Hz, SAs for cluster A align with mean  
445 GMPE predictions for the stations BIM and SAM, whereas they are closer to lower limit of  
446 GMPE predictions for the other two stations. At 5 Hz, the cluster B mostly overestimates the  
447 GMPE predictions for all stations except for MPOM, and the agreement of the first cluster with  
448 GMPE remains station dependent. The comparative analysis of PGA prediction between the  
449 synthetic data and GMPEs gives the same conclusion as we show here for SA at 5 Hz: the  
450 synthetic data in cluster B overestimates the GMPE predictions for all stations, and the cluster  
451 A data mostly fall into the predicted range of GMPEs for only MPOM (Details can be found in  
452 SI).

453 Accounting for the limitation of ground motion modelling above the corner frequency of  
454 EGFs, that equals 5 Hz, we further verified our conclusions below that frequency. Our conclu-  
455 sions remain valid: ground motion amplitude is clustered in two groups, and the compatibility  
456 of the clusters with the GMPEs depends on both station and evaluated frequency (detailed in  
457 SI).

### 458 **4.3 EGF selection can emerge as a significant station-dependent factor for ground** 459 **motion prediction**

460 The third question we aimed to address is: ‘Does EGF selection further influence ground motion  
461 estimations?’ The analyses in previous sections were based on the multi-EGF approach in order

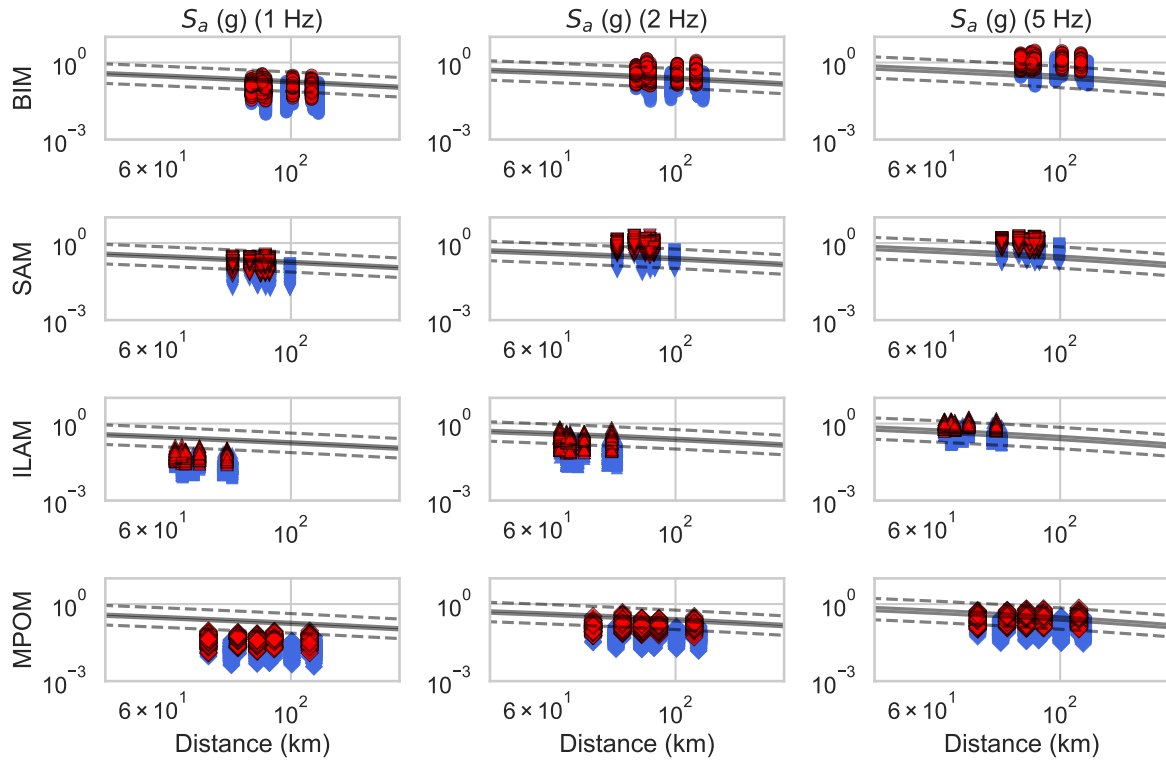


**Figure 9.** Comparison of cluster A (in blue) and cluster B (in red) cases of synthetic ground motion with GMPE curves from Zhao et al. (2006) (in gray) by spectral acceleration at 1 Hz (left panel), 2 Hz (mid-panel), and 5 Hz (right panel). The results for 5 Hz Mean GMPE curves are shown in solid lines; the lower and upper limits of GMPE curves are shown in dashed lines. Each row stands for the analysis of a station: BIM, SAM, ILAM, and MPOM from top to bottom, respectively. We used soil class #4 for GMPEs.

462 to focus exclusively on the source effects. Here we explore the role of the EGF selection by  
 463 repeating the logic tree simulations for each single-EGF use.

464 We found that the predicted ground motion can be highly sensitive to EGF selection: the  
 465 energy difference of EGFs in a specific frequency band can cause significant variations in pre-  
 466 dicted ground motion despite the EGF corrections. We categorised the synthetic data by EGF  
 467 use as shown in Fig. 10. Stations BIM, ILAM, and MPOM exhibit notably higher ground mo-  
 468 tion amplitudes for the use of EGF III, while for station SAM, such effect is not obvious.

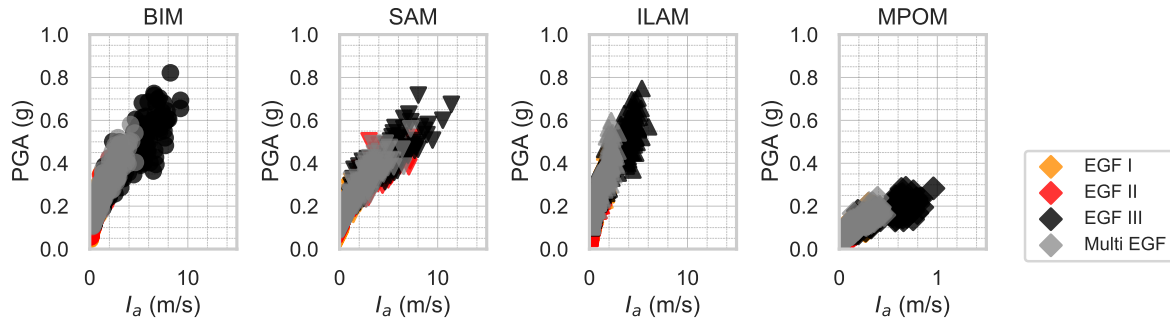


**Figure 10.** Effect of EGF selection on ground motion. Comparison of peak ground acceleration vs peak Arias intensity results between all EGF approaches. Each diagram shows the results for a station.

## 5 DISCUSSION

### 5.1 Variation of ground motion between stations

The range of ground motion amplitude strongly varies between the four stations; In general, we computed a weaker ground motion amplitude for station MPOM compared to other stations. Fig. 11 shows histograms and kernel density estimations (KDE) of computed PGA for all performed simulations. KDE is a way of visualising the shape of the sample distribution (Parzen 1962; Davis et al. 2011); it is defined as the normalised sum of kernel functions of a certain width computed on the data samples (here we use Gaussian kernels of standard deviation 0.10, 0.10, 0.11, and 0.04 g for stations BIM, SAM, ILAM, and MPOM, respectively; details on KDE can be found in the reference provided in Data and resources). The results point to a similarity between three stations, BIM, SAM and ILAM, in terms of amplitude and standard deviation. For both clusters, the mean values for the three stations are roughly twice as that of MPOM. For example, the mean PGA of the cluster A ranges between 0.2 and 0.22 g for the three stations, whereas this value lowers to 0.08 g for station MPOM. The peak kernel density notably increases, approximately twice, at station MPOM due to the narrow range of PGA, i.e., limited variation, compared to the other three stations.

A detailed site characterisation is essential to better assess the variation potential of ground motion between the stations and understand the reason behind it. Recall that we found that the significance of ground motion variation with respect to GMPE and the potential of further variation due to EGF selection are station-dependent. Our current knowledge about site conditions is

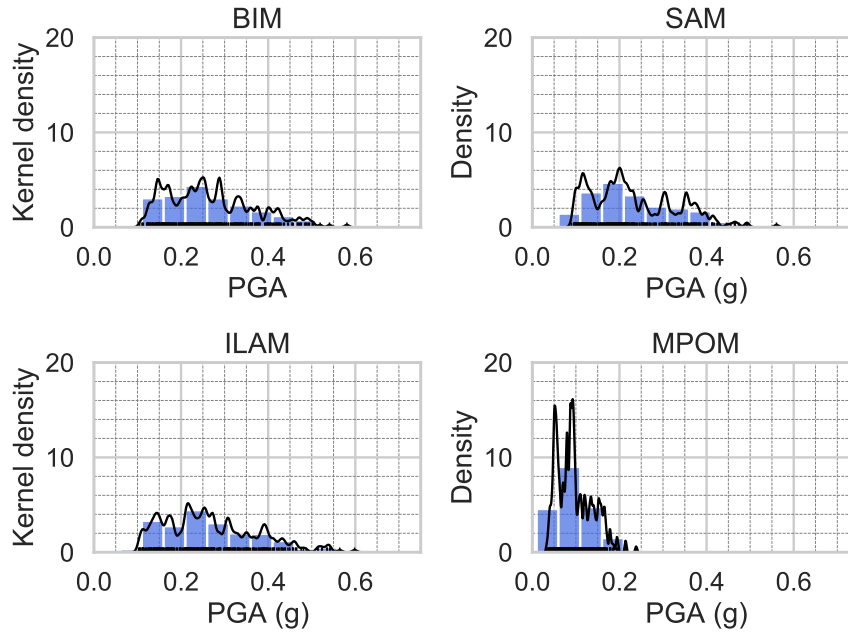


**Figure 11.** Histograms of peak ground acceleration values at each station, associated with kernel density (black curve). Each rug stands for a simulation result.

489 limited and does not allow for further interpretations of the variation of ground motion between  
 490 stations in our results. Additional analyses to characterise site effects at Martinique stations—as  
 491 applied in Guadeloupe (Castro et al. 2003)—would be helpful for future seismic hazard studies  
 492 in Martinique. Moreover, EGF method considers a similarity of the source-to-site propagation  
 493 path between EGF and target earthquake; it cannot account for further variation of ground mo-  
 494 tion due to possible site-related complexities due to a strong earthquake. We target a magnitude  
 495 7.5 earthquake, and further variation of ground motion due to complex soil behaviour (e.g., soil  
 496 nonlinearity, and liquefaction) under such a strong earthquake is possible as known by past ob-  
 497 servations and numerical studies (e.g., Aguirre & Irikura 1997; Ghofrani et al. 2013; Régnier  
 498 et al. 2013; Oral et al. 2019). Further research on this aspect, together with an enhanced site  
 499 characterisation, can take the effort of ground motion prediction a step forward.

## 500 5.2 Need for an improved regional GMPE

501 The absence of a regional GMPE for a magnitude 7.5 earthquake is another limitation for the  
 502 interpretation of our results; the only regional GMPE, the ‘B3’ model (Beauducel et al. 2011),  
 503 also needs revision for moderate events. Here we used the GMPE of Zhao et al. (2006), that was

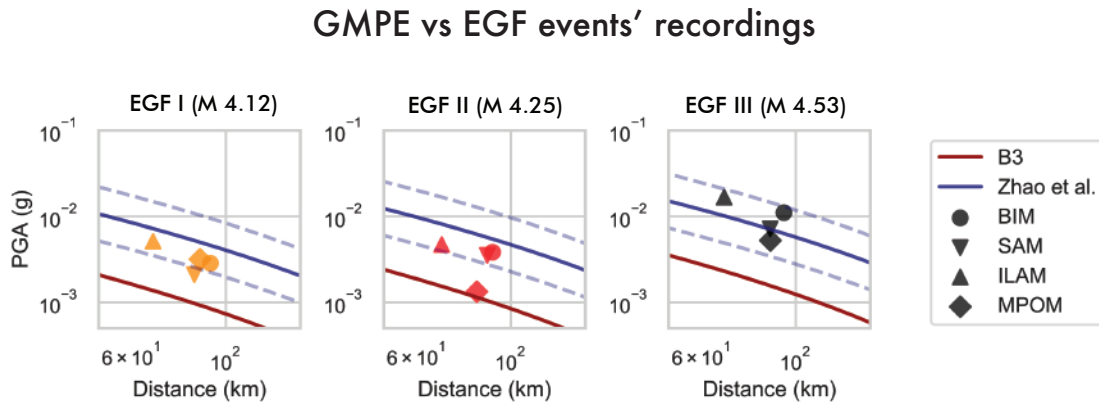


**Figure 12.** Comparison of recorded PGA to GMPE estimations for the three EGF events at the four Martinique stations. [Zhao et al. \(2006\)](#) model is in blue (with lower and upper limits as dashed lines), whereas the B3 model ([Beauducel et al. 2011](#)) is in red.

504 developed with Japanese data, to analyse our synthetic ground motion data, since the B3 model  
 505 is not recommended for  $M \geq 6.5$  earthquakes. Although past studies qualify the [Zhao et al.](#)  
 506 (2006) GMPE as the best representative of our target earthquake, [Kotha \(2018\)](#) states that the  
 507 use of a GMPE that has been developed with the data from a different region can become non-  
 508 ergodic due to the differences of crustal characteristics. Therefore, according to the latter, such  
 509 GMPEs require additional adjustments of ground motion before application to other regions. In  
 510 that sense, future mitigation studies would benefit from further research on GMPE applications.

511 We compared the B3 model and [Zhao et al. \(2006\)](#) GMPE with the EGF recordings, in a  
 512 range of magnitudes (4.2–4.5) where both GMPEs are valid (Fig. 12). B3 model underestimates  
 513 all the three events, whereas [Zhao et al. \(2006\)](#) is mostly in agreement with observations. This  
 514 incompatibility also points to further need to improve regional GMPE applications.

## 515 6 CONCLUSIONS

516 A  $M > 7$  interplate earthquake is expected offshore Martinique. In this study, we investigated  
 517 the most influential parameters on broadband ground motion mainly due to source kinematics  
 518 for a hypothetical  $M_w$  7.5 earthquake.

519 Our findings are:

520 (i) The fault geometry and the spatial extension of the largest slip patch are the most deter-

521 minant source-related factors for ground motion. The combination of a rectangular fault with a  
522 high aspect ratio and condensed small slip asperities can result in a significant amplification of  
523 source energy. Such energy amplification manifests itself by a substantial increase of broadband  
524 wave energy and ground motion amplitude throughout the signal duration. We stress that we set  
525 the down-dip limit to 55 km, as suggested by [Paulatto et al. \(2017\)](#) for the coupled interface of  
526 the subduction zone; more studies are needed to constrain the further role of the fault geometry  
527 when considering different depths of the down-dip limit.

528 (ii) The agreement between simulated ground motion and GMPE estimations is highly sen-  
529 sitive to the evaluated frequency of ground motion and station. Future research on the improve-  
530 ment of regional GMPE application and site characterisation is necessary to constrain the real-  
531 istic range of ground motion and source parameters.

532 (iii) EGF selection can be another factor causing significant variation in the predicted ground  
533 motion. The application of EGF technique for forward modelling in moderately seismic areas  
534 such as Martinique requires a special attention to EGF selection, because of potential energy  
535 differences between EGF events. Despite the broadband ground motion modelling (0.5-25 Hz),  
536 we underline that the variability of our results is higher beyond the EGF corner frequency, that  
537 equals 5 Hz here, because of the stochastic nature of rupture at those frequencies. Thus, we put  
538 a special emphasis on the need for using more EGFs and a deeper look to rupture dynamics to  
539 better constrain the ground motion at such high frequencies.

## 540 **ACKNOWLEDGEMENTS**

541 This study is funded by the convention between Institut de Physique du Globe de Paris and  
542 General Directorate of Prevention of Risks of French Ministry for the Ecological and Inclusive  
543 Transition and by the project "Vers la Plateforme Régionale de Surveillance Tellurique du futur"  
544 (PREST) co-funded by INTERREG Caraïbes for the European Regional Development Fund.

545 We would like thank to Sergio Del Gaudio, František Gallovič, and Jean-Marie Saurel for  
546 their substantial help in applying the method of multi-EGF, using the RIK model, and in re-  
547 trieval of the seismic catalogue of the Lesser Antilles, respectively. We also acknowledge —

548 in chronological order — the fruitful discussions with Pascal Bernard, Luis Fabian Bonilla,  
549 Pierre-Yves Bard, and Jean-Paul Ampuero that definitely improved the quality of this work.

550 We would also like to thank Gaetano Festa and the anonymous reviewer for their construc-  
551 tive remarks which helped improving this manuscript.

## 552 Data and resources

553 The seismic catalogue for Lesser Antilles used in this study is available from [OVSG & OVSM](#)  
554 (2020). Note that event `ipgp2017hushqx` is not present in the catalogue, since it has been  
555 superseded by event `ipgp2017hushqz` (see discussion in [EGF selection](#)).

556 Waveform data from networks G, WI, GL and MQ ([IPGP & EOST 1982](#); [IPGP 2008c,a,b](#))  
557 was downloaded from the IPGP Data Center (<http://datacenter.ipgp.fr>).

558 Waveform data from networks CU and NA ([Albuquerque Seismological Laboratory \(ASL\)/USGS](#)  
559 [2006](#); [KNMI 2006](#)) was obtained through the IRIS Data Management Center ([https://ds.](https://ds.iris.edu/ds/nodes/dmc/)  
560 [iris.edu/ds/nodes/dmc/](https://ds.iris.edu/ds/nodes/dmc/)).

561 The RIKsrf code, used for modelling kinematic source rupture, is available at [https://](https://github.com/fgallovic/RIKsrf)  
562 [github.com/fgallovic/RIKsrf](https://github.com/fgallovic/RIKsrf). The SourceSpec code, used to determine earthquake source  
563 parameters, is available at <https://github.com/SeismicSource/sourcespec>.

564 Data analysis has been performed using ObsPy ([Krischer et al. 2015](#)). Figures have been  
565 produced using the Generic Mapping Tools ([Wessel et al. 2019](#)) and Matplotlib ([Hunter 2007](#)).

566 Explanation of seaborn library tools of Python to visualise kernel density plots can be  
567 found at <https://seaborn.pydata.org/tutorial/distributions.html> and [https://](https://mathisonian.github.io/kde/)  
568 [mathisonian.github.io/kde/](https://mathisonian.github.io/kde/).

## 569 REFERENCES

- 570 Aguirre, J. & Irikura, K., 1997. Nonlinearity, liquefaction, and velocity variation of soft soil layers in  
571 Port Island, Kobe, during the Hyogo-ken Nanbu earthquake, *Bulletin of the Seismological society of*  
572 *America*, **87**(5), 1244–1258.
- 573 Aki, K., 1967. Scaling law of seismic spectrum, *Journal of Geophysical Research*, **72**(4), 1217–1231,  
574 doi: [10.1029/JZ072i004p01217](https://doi.org/10.1029/JZ072i004p01217).
- 575 Aki, K. & Richards, P., 2002. *Quantitative Seismology*, University Science Books.



- 576 Albuquerque Seismological Laboratory (ASL)/USGS, 2006. Caribbean usgs network, doi:  
577 [10.7914/SN/CU](https://doi.org/10.7914/SN/CU).
- 578 Ameri, G., Gallovič, F., Pacor, F., & Emolo, A., 2009. Uncertainties in strong ground-motion prediction  
579 with finite-fault synthetic seismograms: An application to the 1984 M 5.7 Gubbio, central Italy, earth-  
580 quake, *Bulletin of the Seismological Society of America*, **99**(2A), 647–663, doi: [10.1785/0120080240](https://doi.org/10.1785/0120080240).
- 581 Andrews, D., 1980. A stochastic fault model: 1. static case, *Journal of Geophysical Research: Solid*  
582 *Earth*, **85**(B7), 3867–3877.
- 583 Anglade, A., Lemarchand, A., Saurel, J.-M., Clouard, V., Bouin, M.-P., Chabalier, J.-B. D., Tait, S.,  
584 Brunet, C., Nercessian, A., Beauducel, F., Robertson, R., Lynch, L., Higgins, M., & Latchman, J.,  
585 2015. Significant technical advances in broadband seismic stations in the Lesser Antilles, *Advances*  
586 *in Geosciences*, **40**, 43–50, doi: [10.5194/adgeo-40-43-2015](https://doi.org/10.5194/adgeo-40-43-2015).
- 587 Audru, J. C., Vernier, J. L., Capdeville, B., Salindre, J. J., & Mouly, E., 2013. Preparedness actions  
588 towards seismic risk mitigation for the general public in Martinique, French Lesser Antilles: a mid-  
589 term appraisal, *Natural Hazards and Earth System Sciences*, **13**(8), 2031–2039, doi: [10.5194/nhess-](https://doi.org/10.5194/nhess-13-2031-2013)  
590 [13-2031-2013](https://doi.org/13-2031-2013).
- 591 Barbot, S., 2020. Frictional and structural controls of seismic super-cycles at the japan trench, *Earth,*  
592 *Planets and Space*, **72**(1), doi: [10.1186/s40623-020-01185-3](https://doi.org/10.1186/s40623-020-01185-3).
- 593 Beauducel, F., Bazin, S., Bengoubou-Valerius, M., Bouin, M.-P., Bosson, A., Anténor-Habazac, C.,  
594 Clouard, V., & De Chabalier, J.-B., 2011. Empirical model for rapid macroseismic intensities pre-  
595 diction in Guadeloupe and Martinique, *Comptes Rendus Géoscience*, **343**(11-12), 717–728, doi:  
596 [10.1016/j.crte.2011.09.004](https://doi.org/10.1016/j.crte.2011.09.004).
- 597 Bozzoni, F., Corigliano, M., Lai, C. G., Salazar, W., Scandella, L., Zuccolo, E., Latchman, J., Lynch,  
598 L., & Robertson, R., 2011. Probabilistic seismic hazard assessment at the Eastern Caribbean Islands,  
599 *Bulletin of the seismological society of America*, **101**(5), 2499–2521, doi: [10.1785/0120100208](https://doi.org/10.1785/0120100208).
- 600 Brune, J. N., 1970. Tectonic stress and the spectra of seismic shear waves from earthquakes, *Journal of*  
601 *Geophysical Research*, **75**(26), 4997–5009, doi: [10.1029/JB075i026p04997](https://doi.org/10.1029/JB075i026p04997).
- 602 Bureau de recherches géologiques et minières, 2018. Cartes géologiques imprimées des outre-mer,  
603 <https://infoterre.brgm.fr>.
- 604 Castro, R. R., Fabriol, H., Bour, M., & Le Brun, B., 2003. Attenuation and site effects in the region of  
605 Guadeloupe, Lesser Antilles, *Bulletin of the Seismological Society of America*, **93**(2), 612–626, doi:  
606 [10.1785/0120020042](https://doi.org/10.1785/0120020042).
- 607 Causse, M., Chaljub, E., Cotton, F., Cornou, C., & Bard, P.-Y., 2009. New approach for coupling  $k^{-2}$   
608 and empirical Green's functions: application to the blind prediction of broad-band ground motion  
609 in the Grenoble basin, *Geophysical Journal International*, **179**(3), 1627–1644, doi: [10.1111/j.1365-](https://doi.org/10.1111/j.1365-246X.2009.04354.x)  
610 [246X.2009.04354.x](https://doi.org/246X.2009.04354.x).
- 611 Causse, M., Cultrera, G., Moreau, L., Herrero, A., Schiappapietra, E., & Courboux, F., 2017. Bayesian  
612 rupture imaging in a complex medium: The 29 May 2012 Emilia, Northern Italy, earthquake, *Geophys-*

- 613 *ical Research Letters*, **44**(15), 7783–7792, doi: [10.1002/2017GL074698](https://doi.org/10.1002/2017GL074698).
- 614 Courboux, F., Converset, J., Balestra, J., & Delouis, B., 2010. Ground-motion simulations of the 2004  
615 Mw 6.4 Les Saintes, Guadeloupe, earthquake using ten smaller events, *Bulletin of the Seismological*  
616 *Society of America*, **100**(1), 116–130, doi: [10.1785/0120080372](https://doi.org/10.1785/0120080372).
- 617 Davis, R. A., Lii, K.-S., & Politis, D. N., 2011. Remarks on some nonparametric estimates  
618 of a density function, in *Selected Works of Murray Rosenblatt*, pp. 95–100, Springer, doi:  
619 [10.1214/aoms/1177728190](https://doi.org/10.1214/aoms/1177728190).
- 620 Del Gaudio, S., Causse, M., & Festa, G., 2015. Broad-band strong motion simulations coupling k-  
621 square kinematic source models with empirical Green’s functions: the 2009 L’Aquila earthquake,  
622 *Geophysical Journal International*, **203**(1), 720–736, doi: [10.1093/gji/ggv325](https://doi.org/10.1093/gji/ggv325).
- 623 Del Gaudio, S., Hok, S., Festa, G., Causse, M., & Lancieri, M., 2018. Near-fault broadband ground mo-  
624 tion simulations using empirical Green’s functions: Application to the Upper Rhine Graben (France–  
625 Germany) case study, in *Best Practices in Physics-based Fault Rupture Models for Seismic Hazard*  
626 *Assessment of Nuclear Installations*, pp. 155–177, Springer, doi: [10.1007/s00024-017-1575-1](https://doi.org/10.1007/s00024-017-1575-1).
- 627 DeMets, C., Gordon, R. G., & Argus, D. F., 2010. Geologically current plate motions, *Geophysical*  
628 *Journal International*, **181**(1), 1–80, doi: [10.1111/j.1365-246x.2009.04491.x](https://doi.org/10.1111/j.1365-246x.2009.04491.x).
- 629 Douglas, J., 2003. Earthquake ground motion estimation using strong-motion records: a review of equa-  
630 tions for the estimation of peak ground acceleration and response spectral ordinates, *Earth-Science*  
631 *Reviews*, **61**(1-2), 43–104, doi: [10.1016/S0012-8252\(02\)00112-5](https://doi.org/10.1016/S0012-8252(02)00112-5).
- 632 Douglas, J. & Mohais, R., 2009. Comparing predicted and observed ground motions from subduction  
633 earthquakes in the Lesser Antilles, *Journal of seismology*, **13**(4), 577–587, doi: [10.1007/s10950-008-](https://doi.org/10.1007/s10950-008-9150-y)  
634 [9150-y](https://doi.org/10.1007/s10950-008-9150-y).
- 635 Dujardin, A., Causse, M., Courboux, F., & Traversa, P., 2016. Simulation of the basin effects in the Po  
636 Plain during the Emilia-Romagna seismic sequence (2012) using empirical Green’s functions, *Pure*  
637 *and Applied Geophysics*, **173**(6), 1993–2010, doi: [10.1007/s00024-015-1233-4](https://doi.org/10.1007/s00024-015-1233-4).
- 638 Dziewonski, A. M., Chou, T.-A., & Woodhouse, J. H., 1981. Determination of earthquake source  
639 parameters from waveform data for studies of global and regional seismicity, *Journal of Geophysical*  
640 *Research: Solid Earth*, **86**(B4), 2825–2852, doi: [10.1029/jb086ib04p02825](https://doi.org/10.1029/jb086ib04p02825).
- 641 Ekström, G., Nettles, M., & Dziewoński, A., 2012. The global CMT project 2004–2010: Centroid-  
642 moment tensors for 13, 017 earthquakes, *Physics of the Earth and Planetary Interiors*, **200-201**, 1–9,  
643 doi: [10.1016/j.pepi.2012.04.002](https://doi.org/10.1016/j.pepi.2012.04.002).
- 644 Eshelby, J. D., 1957. The determination of the elastic field of an ellipsoidal inclusion, and related  
645 problems, *Proceedings of the Royal Society of London A: Mathematical, Physical and Engineering*  
646 *Sciences*, **241**(1226), 376–396, doi: [10.1098/rspa.1957.0133](https://doi.org/10.1098/rspa.1957.0133).
- 647 Feuillet, N., Beauducel, F., & Tapponnier, P., 2011. Tectonic context of moderate to large historical  
648 earthquakes in the Lesser Antilles and mechanical coupling with volcanoes, *Journal of Geophysical*  
649 *Research: Solid Earth*, **116**(B10), doi: [10.1029/2011JB008443](https://doi.org/10.1029/2011JB008443).

- 650 Frankel, A., 1991. High-frequency spectral falloff of earthquakes, fractal dimension of complex rupture,  
651 b value, and the scaling of strength on faults, *Journal of Geophysical Research: Solid Earth*, **96**(B4),  
652 6291–6302.
- 653 Gallovič, F., 2016. Modeling velocity recordings of the Mw 6.0 South Napa, California, earthquake:  
654 Unilateral event with weak high-frequency directivity, *Seismological Research Letters*, **87**(1), 2–14,  
655 doi: [10.1785/0220150042](https://doi.org/10.1785/0220150042).
- 656 Ghofrani, H., Atkinson, G. M., & Goda, K., 2013. Implications of the 2011 M9.0 Tohoku Japan earth-  
657 quake for the treatment of site effects in large earthquakes, *Bulletin of Earthquake Engineering*, **11**(1),  
658 171–203, doi: [10.1007/s10518-012-9413-4](https://doi.org/10.1007/s10518-012-9413-4).
- 659 Hartzell, S., Leeds, A., Frankel, A., Williams, R. A., Odum, J., Stephenson, W., & Silva, W., 2002. Sim-  
660 ulation of broadband ground motion including nonlinear soil effects for a magnitude 6.5 earthquake  
661 on the Seattle fault, Seattle, Washington, *Bulletin of the Seismological Society of America*, **92**(2),  
662 831–853, doi: [10.1785/0120010114](https://doi.org/10.1785/0120010114).
- 663 Hartzell, S. H., 1978. Earthquake aftershocks as Green's functions, *Geophysical Research Letters*, **5**(1),  
664 1–4, doi: [10.1029/GL005i001p00001](https://doi.org/10.1029/GL005i001p00001).
- 665 Hunter, J. D., 2007. Matplotlib: A 2D graphics environment, *Computing in Science & Engineering*,  
666 **9**(3), 90–95, doi: [10.1109/MCSE.2007.55](https://doi.org/10.1109/MCSE.2007.55).
- 667 Hutchings, L. & Viegas, G., 2012. Application of empirical green's functions in earthquake source,  
668 wave propagation and strong ground motion studies, *Earthquake Research and Analysis-New Fron-*  
669 *tiers in Seismology*.
- 670 Hutchings, L., Ioannidou, E., Foxall, W., Voulgaris, N., Savy, J., Kalogeras, I., Scognamiglio, L., &  
671 Stavrakakis, G., 2007. A physically based strong ground-motion prediction methodology; application  
672 to PSHA and the 1999  $M_w = 6.0$  Athens earthquake, *Geophysical Journal International*, **168**(2),  
673 659–680, doi: [10.1111/j.1365-246X.2006.03178.x](https://doi.org/10.1111/j.1365-246X.2006.03178.x).
- 674 Imperatori, W. & Mai, P. M., 2012. Sensitivity of broad-band ground-motion simulations to earthquake  
675 source and Earth structure variations: an application to the Messina Straits (Italy), *Geophysical Journal*  
676 *International*, **188**(3), 1103–1116, doi: [10.1111/j.1365-246X.2011.05296.x](https://doi.org/10.1111/j.1365-246X.2011.05296.x).
- 677 IPGP, 2008a. Seismic, deformation, gas, magnetic and weather permanent networks on soufrière vol-  
678 cano and guadeloupe island, doi: [10.18715/GUADELOUPE.GL](https://doi.org/10.18715/GUADELOUPE.GL).
- 679 IPGP, 2008b. Seismic, deformation, gas, magnetic and weather permanent networks on mount pelée  
680 volcano and martinique island, doi: [10.18715/MARTINIQUE.MQ](https://doi.org/10.18715/MARTINIQUE.MQ).
- 681 IPGP, 2008c. Gns, seismic broadband and strong motion permanent networks in west indies, doi:  
682 [10.18715/ANTILLES.WI](https://doi.org/10.18715/ANTILLES.WI).
- 683 IPGP & EOST, 1982. Geoscope, french global network of broad band seismic stations, doi:  
684 [10.18715/GEOSCOPE.G](https://doi.org/10.18715/GEOSCOPE.G).
- 685 Irikura, K., 1986. Prediction of strong acceleration motion using empirical Green's function, in *Proc.*  
686 *7th Japan Earthq. Eng. Symp.*, vol. 151, pp. 151–156, available from <http://www.kojiro-irikura>.

- 687 [jp/pdf/7th\\_J\\_Earthquake\\_Eng\\_Sympo.pdf](#).
- 688 Kamae, K. & Irikura, K., 1998. Source model of the 1995 Hyogo-ken Nanbu earthquake and simulation  
689 of near-source ground motion, *Bulletin of the Seismological Society of America*, **88**(2), 400–412.
- 690 KNMI, 2006. Caribbean netherlands seismic network, doi: [10.21944/DFFA7A3F-7E3A-3B33-A436-](https://doi.org/10.21944/DFFA7A3F-7E3A-3B33-A436-516A01B6AF3F)  
691 [516A01B6AF3F](https://doi.org/10.21944/DFFA7A3F-7E3A-3B33-A436-516A01B6AF3F).
- 692 Kotha, S. R., 2018. *Quantification of uncertainties in seismic ground-motion prediction*, Ph.D.  
693 thesis, Universität Potsdam Potsdam, [http://nbn-resolving.de/urn/resolver.pl?urn=urn:](http://nbn-resolving.de/urn/resolver.pl?urn=urn:nbn:de:kobv:517-opus4-415743)  
694 [nbn:de:kobv:517-opus4-415743](http://nbn-resolving.de/urn/resolver.pl?urn=urn:nbn:de:kobv:517-opus4-415743).
- 695 Krischer, L., Megies, T., Barsch, R., Beyreuther, M., Lecocq, T., Caudron, C., & Wassermann, J., 2015.  
696 ObsPy: a bridge for seismology into the scientific Python ecosystem, *Computational Science & Dis-*  
697 *covery*, **8**(1), 014003, doi: [10.1088/1749-4699/8/1/014003](https://doi.org/10.1088/1749-4699/8/1/014003).
- 698 Laigle, M., Hirn, A., Sapin, M., Bécel, A., Charvis, P., Flueh, E., Diaz, J., Lebrun, J.-F., Gesret, A.,  
699 Raffaele, R., et al., 2013. Seismic structure and activity of the north-central Lesser Antilles subduction  
700 zone from an integrated approach: Similarities with the Tohoku forearc, *Tectonophysics*, **603**, 1–20,  
701 doi: [10.1016/j.tecto.2013.05.043](https://doi.org/10.1016/j.tecto.2013.05.043).
- 702 Lancieri, M., Renault, M., Berge-Thierry, C., Gueguen, P., Baumont, D., & Perrault, M., 2015. Strategy  
703 for the selection of input ground motion for inelastic structural response analysis based on naïve  
704 Bayesian classifier, *Bulletin of Earthquake Engineering*, **13**(9), 2517–2546, doi: [10.1007/s10518-015-](https://doi.org/10.1007/s10518-015-9728-z)  
705 [9728-z](https://doi.org/10.1007/s10518-015-9728-z).
- 706 Madariaga, R. & Ruiz, S., 2016. Earthquake dynamics on circular faults: A review 1970–2015, *Journal*  
707 *of Seismology*, **20**(4), 1235–1252, doi: [10.1007/s10950-016-9590-8](https://doi.org/10.1007/s10950-016-9590-8).
- 708 McGuire, J. & Ben-Zion, Y., 2017. Detailed analysis of earthquake directivity in the San Jacinto Fault  
709 Zone, *SCEC Final Report, Project 16104*, <https://www.scec.org/proposal/report/16104>.
- 710 Oral, E., Gélis, C., & Bonilla, L. F., 2019. 2-D P-SV and SH spectral element modelling of seismic  
711 wave propagation in non-linear media with pore-pressure effects, *Geophysical Journal International*,  
712 **217**(2), 1353–1365, doi: [10.1093/gji/ggz041](https://doi.org/10.1093/gji/ggz041).
- 713 OVSG & OVSM, 2020. Unified seismic catalogue for the Lesser Antilles, 2014-2019, doi:  
714 [10.18715/IPGP.2020.kgmbivor](https://doi.org/10.18715/IPGP.2020.kgmbivor).
- 715 Pacor, F., Ameri, G., Gallovic, F., & D'Amico, M., 2017. Ground motion variability from finite fault  
716 simulations, in *Proceedings of the 16th World Conference on Earthquake (16WCEE), Santiago, Chile*,  
717 pp. 9–13.
- 718 Parzen, E., 1962. On estimation of a probability density function and model, *Annals of Mathematical*  
719 *Statistics*, **33**(3), 1065–1076, doi: [10.1214/aoms/1177704472](https://doi.org/10.1214/aoms/1177704472).
- 720 Paulatto, M., Laigle, M., Galve, A., Charvis, P., Sapin, M., Bayrakci, G., Evain, M., & Kopp, H., 2017.  
721 Dehydration of subducting slow-spread oceanic lithosphere in the Lesser Antilles, *Nature communi-*  
722 *cations*, **8**, 15980, doi: [10.1038/ncomms15980](https://doi.org/10.1038/ncomms15980).
- 723 Pavic, R., Koller, M. G., Bard, P.-Y., & Lacave-Lachet, C., 2000. Ground motion prediction with the

- 724 empirical Green's function technique: an assessment of uncertainties and confidence level, *Journal of*  
725 *Seismology*, **4**(1), 59–77, doi: [10.1023/A:1009826529269](https://doi.org/10.1023/A:1009826529269).
- 726 Pulido, N., Ojeda, A., Atakan, K., & Kubo, T., 2004. Strong ground motion estimation in the Sea of  
727 Marmara region (Turkey) based on a scenario earthquake, *Tectonophysics*, **391**(1-4), 357–374, doi:  
728 [10.1016/j.tecto.2004.07.023](https://doi.org/10.1016/j.tecto.2004.07.023).
- 729 Ragon, T., Sladen, A., & Simons, M., 2019. Accounting for uncertain fault geometry in earthquake  
730 source inversions—II: application to the  $M_w$  6.2 Amatrice earthquake, central Italy, *Geophysical Jour-*  
731 *nal International*, **218**(1), 689–707, doi: [10.1093/gji/ggz180](https://doi.org/10.1093/gji/ggz180).
- 732 Régnier, J., Cadet, H., Bonilla, L. F., Bertrand, E., & Semblat, J.-F., 2013. Assessing nonlinear behavior  
733 of soils in seismic site response: Statistical analysis on KiK-net strong-motion data, *Bulletin of the*  
734 *Seismological Society of America*, **103**(3), 1750–1770, doi: [10.1785/0120120240](https://doi.org/10.1785/0120120240).
- 735 Ripperger, J., Mai, P., & Ampuero, J.-P., 2008. Variability of near-field ground motion from dynamic  
736 earthquake rupture simulations, *Bulletin of the seismological society of America*, **98**(3), 1207–1228,  
737 doi: [10.1785/0120070076](https://doi.org/10.1785/0120070076).
- 738 Ruiz, J., Baumont, D., Bernard, P., & Berge-Thierry, C., 2011. Modelling directivity of strong ground  
739 motion with a fractal,  $k^{-2}$ , kinematic source model, *Geophysical Journal International*, **186**(1), 226–  
740 244, doi: [10.1111/j.1365-246X.2011.05000.x](https://doi.org/10.1111/j.1365-246X.2011.05000.x).
- 741 Ruiz, M., Galve, A., Monfret, T., Sapin, M., Charvis, P., Laigle, M., Evain, M., Hirn, A., Flueh, E.,  
742 Gallart, J., et al., 2013. Seismic activity offshore Martinique and Dominica islands (Central Lesser  
743 Antilles subduction zone) from temporary onshore and offshore seismic networks, *Tectonophysics*,  
744 **603**, 68–78, doi: [10.1016/j.tecto.2011.08.006](https://doi.org/10.1016/j.tecto.2011.08.006).
- 745 Russo, R. M., Okal, E. A., & Rowley, K. C., 1992. Historical seismicity of the southeastern Caribbean  
746 and tectonic implications, *Pure and Applied Geophysics*, **139**(1), 87–120, doi: [10.1007/BF00876827](https://doi.org/10.1007/BF00876827).
- 747 Satriano, C., 2020. SourceSpec – Earthquake source parameters from S-wave displacement spectra,  
748 doi: [10.5281/ZENODO.3688587](https://doi.org/10.5281/ZENODO.3688587).
- 749 Satriano, C., Dionicio, V., Miyake, H., Uchida, N., Vilotte, J.-P., & Bernard, P., 2014. Structural and  
750 thermal control of seismic activity and megathrust rupture dynamics in subduction zones: Lessons  
751 from the  $M_w$  9.0, 2011 Tohoku earthquake, *Earth and Planetary Science Letters*, **403**, 287–298, doi:  
752 [10.1016/j.epsl.2014.06.037](https://doi.org/10.1016/j.epsl.2014.06.037).
- 753 Sørensen, M. B., Pulido, N., & Atakan, K., 2007. Sensitivity of ground-motion simulations to earth-  
754 quake source parameters: a case study for Istanbul, Turkey, *Bulletin of the Seismological Society of*  
755 *America*, **97**(3), 881–900, doi: [10.1785/0120060044](https://doi.org/10.1785/0120060044).
- 756 Spudich, P., Cirella, A., Scognamiglio, L., & Tinti, E., 2019. Variability in synthetic earthquake ground  
757 motions caused by source variability and errors in wave propagation models, *Geophysical Journal*  
758 *International*, **219**(1), 346–372, doi: [10.1093/gji/ggz275](https://doi.org/10.1093/gji/ggz275).
- 759 Vallée, M., Charléty, J., Ferreira, A. M., Delouis, B., & Vergoz, J., 2011. SCARDEC: a new technique  
760 for the rapid determination of seismic moment magnitude, focal mechanism and source time functions

- 761 for large earthquakes using body-wave deconvolution, *Geophysical Journal International*, **184**(1),  
762 338–358, doi: [10.1111/j.1365-246X.2010.04836.x](https://doi.org/10.1111/j.1365-246X.2010.04836.x).
- 763 Wang, H., Igel, H., Gallovič, F., & Cochard, A., 2009. Source and basin effects on rotational ground  
764 motions: Comparison with translations, *Bulletin of the Seismological Society of America*, **99**(2B),  
765 1162–1173, doi: [10.1785/0120080115](https://doi.org/10.1785/0120080115).
- 766 Weil-Accardo, J., Feuillet, N., Jacques, E., Deschamps, P., Beauducel, F., Cabioch, G., Tapponnier, P.,  
767 Saurel, J.-M., & Galetzka, J., 2016. Two hundred thirty years of relative sea level changes due to  
768 climate and megathrust tectonics recorded in coral microatolls of Martinique (French West Indies),  
769 *Journal of Geophysical Research: Solid Earth*, **121**(4), 2873–2903, doi: [10.1002/2015JB012406](https://doi.org/10.1002/2015JB012406).
- 770 Wessel, P., Luis, J. F., Uieda, L., Scharroo, R., Wobbe, F., Smith, W. H. F., & Tian, D., 2019. The  
771 Generic Mapping Tools Version 6, *Geochemistry, Geophysics, Geosystems*, **20**(11), 5556–5564, doi:  
772 [10.1029/2019gc008515](https://doi.org/10.1029/2019gc008515).
- 773 Withers, K. B., Olsen, K. B., Shi, Z., & Day, S. M., 2019. Validation of Deterministic Broadband  
774 Ground Motion and Variability from Dynamic Rupture Simulations of Buried Thrust Earthquakes  
775 Validation of Deterministic Broadband Ground Motion and Variability, *Bulletin of the Seismological  
776 Society of America*, **109**(1), 212–228, doi: [10.1785/0120180005](https://doi.org/10.1785/0120180005).
- 777 Zhao, J. X., Zhang, J., Asano, A., Ohno, Y., Oouchi, T., Takahashi, T., Ogawa, H., Irikura, K., Thio,  
778 H. K., Somerville, P. G., et al., 2006. Attenuation relations of strong ground motion in Japan using site  
779 classification based on predominant period, *Bulletin of the Seismological Society of America*, **96**(3),  
780 898–913, doi: [10.1785/0120050122](https://doi.org/10.1785/0120050122).